Check for updates

small methods
www.small-methods.com

Ferroelectric–Optoelectronic Hybrid System for Photodetection

*Jie Liu, Li Su, Xinglong Zhang, Dmitry V. Shtansky, and Xiaosheng Fang**

Photodetectors (PDs), as functional devices based on photon-to-electron conversion, are an indispensable component for the next-generation Internet of Things system. The research of advanced and efficient PDs that meet the diverse demands is becoming a major task. Ferroelectric materials can develop a unique spontaneous polarization due to the symmetry-breaking of the unit cell, which is switchable under an external electric field. Ferroelectric polarization field has the intrinsic characteristics of non-volatilization and rewritability. Introducing ferroelectrics to effectively manipulate the band bending and carrier transport can be non-destructive and controllable in the ferroelectric–optoelectronic hybrid systems. Hence, ferroelectric integration offers a promising strategy for high-performance photoelectric detection. This paper reviews the fundamentals of optoelectronic and ferroelectric materials, and their interactions in hybrid photodetection systems. The first section introduces the characteristics and applications of typical optoelectronic and ferroelectric materials. Then, the interplay mechanisms, modulation effects, and typical device structures of ferroelectric–optoelectronic hybrid systems are discussed. Finally, in summary and perspective section, the progress of ferroelectrics integrated PDs is summed up and the challenges of ferroelectrics in the field of optoelectronics are considered.

1. Introduction

With the advent of the Internet of Things era, communication and interaction among systems or between systems and people have become efficient and frequent. Front-end information collection as a part of the IoT system promotes the rapid evolution of electronics and optoelectronic devices. As a receiver, photodetectors (PDs) play an important role in optical communication systems. PDs are a class of sensors converting light into electrical signals, typically in the form of current or voltage. The performance of PDs is evaluated by a series of figures of merit, including responsivity, response speed, detectivity, quantum efficiency, and noise, which are dominated by the device structures and more by the optoelectronic materials. For a long time, conventional semiconductors, such as Si, GaAs, and CdTe, have been applied in optoelectronic detection owing to their stable performance and mature manufacturing process.[1,2] With the ever-growing demands of quantum efficiency, miniaturization, and power consumption, many emerging optoelectronic materials, including 2D materials, perovskites, and organic polymers, have drawn tremendous attention in recent decades.[3–7] Meanwhile, structure design,[8,9] bandgap engineering,[10,11] ultrathin size,[12,13] and other means were employed to reach high-performance PDs. However, the current PDs still have challenges of high dark current, low absorption efficiency, and high cost. Therefore, developing new optoelectronic materials and/or manipulation mechanisms in the detection field is necessary.

Emerging smart functional materials are attracting increasing attention, which could realize the manipulation of device properties by applying electric, magnetic, optical, and stress fields. Among them, ferroelectrics are widely studied due to their robust response, polarization adjustability, and simple structure. Remarkably, due to the electric cloud distribution and/or distortion of the atomic framework (symmetry-breaking of the unit cell), ferroelectrics develop a unique spontaneous polarization, which can be re-oriented by an external electric field. In the past, research on ferroelectric materials has mainly focused on conventional bulk perovskite materials. Due to the critical size effect and structure instability, however, the ferroelectric polarization will be broken at nanoscale, which is a hinder for the application of ferroelectrics in micro-devices. Hence, researchers tend to focus on the ultra-thin ferroelectrics with undegraded polarization. The discovery and development of 2D ferroelectrics and fluorite-structure ferroelectrics have made tremendous progress in solving this problem; stable ferroelectricity was reported in ferroelectric films even down to the 1-unit cell limit.[14] Further, to meet demands for flexible devices, researchers began to pay more attention to the study of polyvinylidene fluoride (PVDF), a representative of flexible ferroelectrics. Meanwhile, to improve ferroelectric properties and crystallinity, other monomeric units are frequently introduced into pure PVDF.

J. Liu, L. Su, X. Zhang, X. Fang
Department of Materials Science
State Key Laboratory of Molecular Engineering of Polymers
Institute of Optoelectronics
Fudan University
Shanghai200438, P. R. China
E-mail: xshfang@fudan.edu.cn
D. V. Shtansky
National University of Science and Technology "MISIS"
Moscow119049, Russia

The ORCID identification number(s) for the author(s) of this article can be found under https://doi.org/10.1002/smtd.202300319

DOI: 10.1002/smtd.202300319

 © 2023 Wiley-VCH GmbH

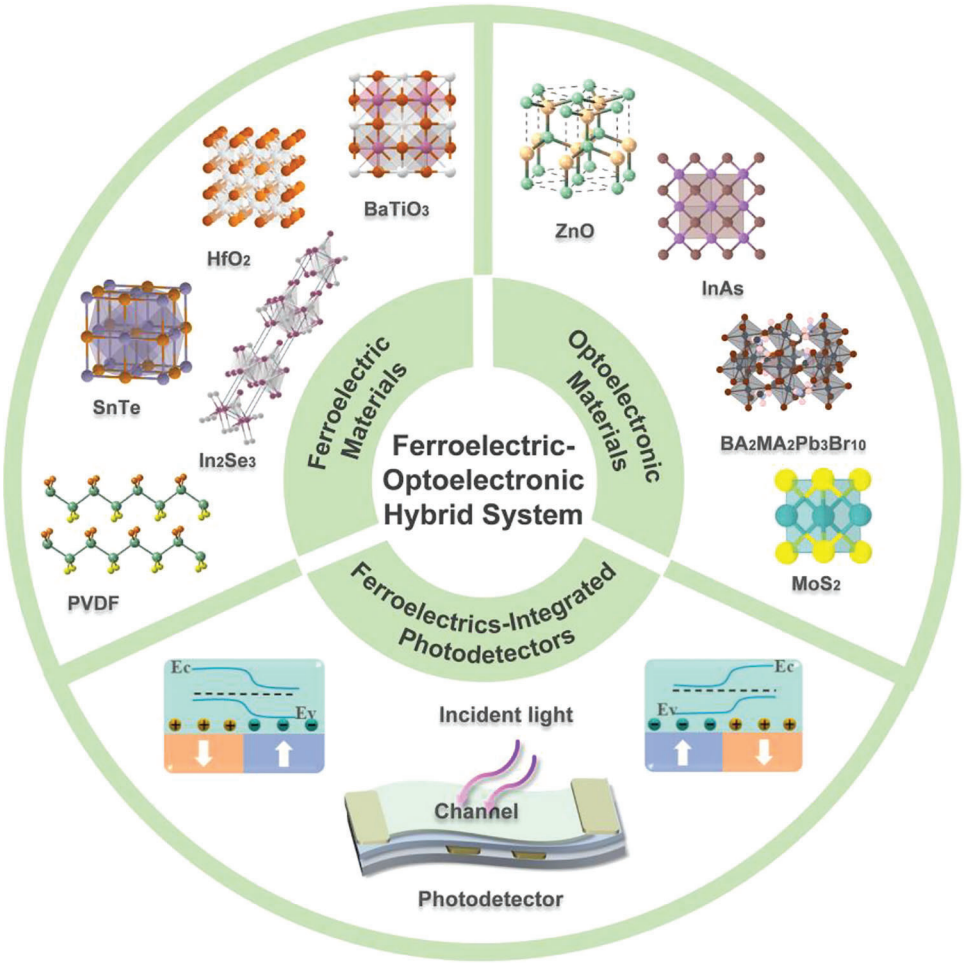

Figure 1. Ferroelectric–optoelectronic system: ferroelectric materials, optoelectronic materials, and ferroelectrics-integrated PDs.

The development of ferroelectrics has promoted their application in electronic devices. Initially, ferroelectrics were often introduced into energy harvesting, non-volatile memories, and logic devices. In the field of optoelectronic detection, it also performed well via manipulation of band alignment and carriers motion. As active layers, some ferroelectrics exhibit great anisotropism in input (e.g., polarized light absorptivity) and output (e.g., migration rate and conductivity in different crystal phases).[15] More importantly, the localized field induced by the ferroelectric polarization effect could suppress the recombination of photogenerated carriers and enhance collection efficiency. Another effective way is that ferroelectrics are integrated into devices to enhance light–matter interaction, band bending, and control carrier motion in a local space. For example, ferroelectrics were employed as gate dielectrics of field-effect transistors (FETs), one end of a heterojunction.[16] FETs is a typical PD structure, whose channel conductance can be tuned by a local interfacial electrostatic field, developed from a programmed ferroelectric field. After the ferroelectric domains are ordered by the applied electric field, the residual polarization of ferroelectrics can achieve a non-volatile localized field. For 2D materials, especially, the tuned p–n junctions can be constructed by creating periodic polarization domains with the aid of an external electric field. Moreover, the ferroelectric polarization doping is controllable and rewritable due to the reversible characteristics. Thus, compared with doping, defect, and surface engineering, the ferroelectric field provides a non-destructive and controllable way to modulate materials properties in the ferroelectric–optoelectronic hybrid systems.

In this article, we review the fundamentals of optoelectronic and ferroelectric materials, and their interactions in the hybrid PDs (**Figure 1**). The characteristics and applications of typical optoelectronic materials were introduced. Meanwhile, we give a detailed summary of ferroelectric materials including the principles, structures, ferroelectric origins and phase transitions, polarization characteristics, and optoelectronic applications. Especially, the modulation mechanisms, integration strategies, and typical device structures of ferroelectrics-integrated PDs are discussed in detail. To sum up, the integration of ferroelectrics has great potential in the field of optoelectronic detection.

2. Introduction of Optoelectronic Materials

At present, the optoelectronic materials for PDs include traditional semiconductor materials, 2D materials, perovskites, and organic materials. In this section, we will provide a brief introduction to the structure, optical and electrical characteristics,

© 2023 Wiley-VCH GmbH

23669608, 0, Downloaded from https://onlinelibrary.wiley.com/doi/10.1002/smtd.202300319 by Fudan University, Wiley Online Library on [28/08/2023]. See the Terms and Conditions (https://onlinelibrary.wiley.com/terms-and-conditions) on Wiley Online Library for rules of use; OA articles are governed by the applicable Creative Commons License

Table 1. Key figures of merit for photodetectors.

Parameter	Unit	Definition	Expression
Responsivity (R)	AW^{-1}	The ratio of photocurrent to the incident light power; the sensitivity of a photodetector to incident light.	$R = \frac{I_p}{P}$ I_p is the photocurrent, P is the light power irradiated on the active area.
External Quantum Efficiency (EQE)	—	The ratio of the number of carriers generated to the number of incident photons; the ability to convert photons into electrical current.	$EQE = \frac{Rhc}{e\lambda} \times 100\%$ h is the Planck constant, c and λ are the velocity and wavelength of light.
Response Time (τ)	s	The time consumption of photocurrent rising from 10% to 90% and decaying from 90% to 10%.	τ_r and τ_d τ_r and τ_d are rising time and decaying time.
Noise Equivalent Power (NEP)	$WHz^{-1/2}$	The ratio of the noise current to the responsivity; the minimum detectable light power that can be distinguished from the background noise.	$NEP = \frac{i_N}{R}$ i_N is noise current.
Detectivity (D^*)	cm $Hz^{1/2}$ W^{-1} (Jones)	The ability of a device for detecting weak signal; an overall measure of device performance.	$D^* = \frac{\sqrt{A\Delta f}}{i_N} R$ A is the active area of photodetectors, Δf is the frequency bandwidth of the detector.
Gain (G)	—	The number of photogenerated carriers per absorbed photon; the amplification of the electrical signal output in response to the incident light.	$G = \frac{\tau_{life}}{\tau_{transit}}$ τ_{life} is the life time of photo generated carriers, $\tau_{transit}$ is the transit time through the channel.

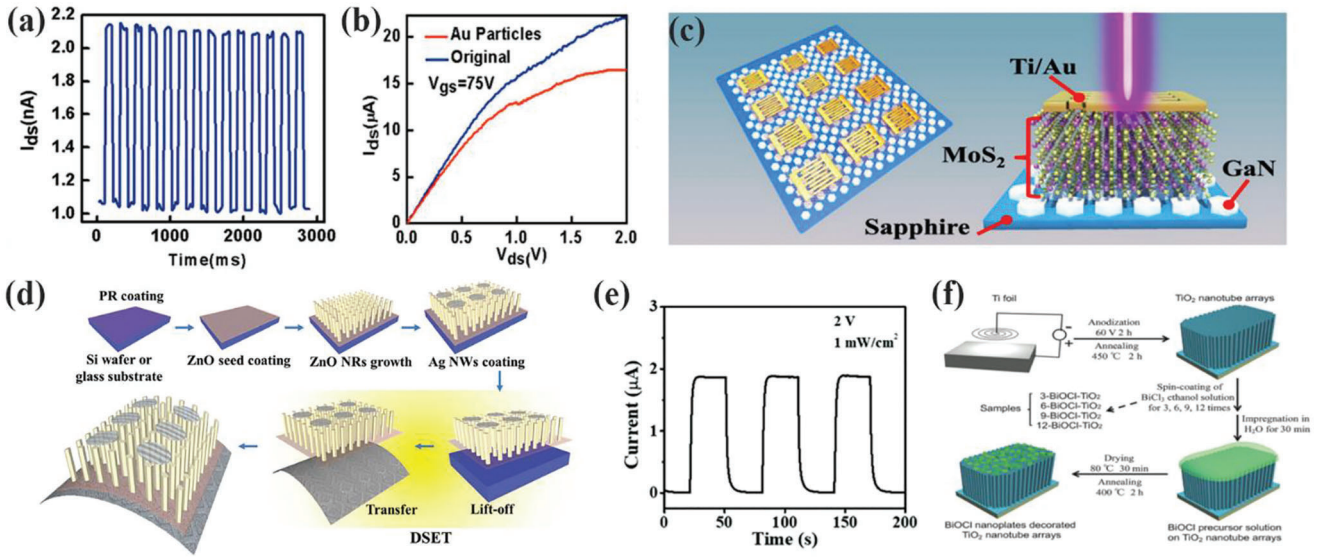

Figure 2. a) Photoresponse of InAs nanowire PDs. b) *I–V* curves of original InAs and Au-decorated InAs PDs. Reproduced with permission.[17] Copyright 2014, American Chemical Society. c) The structure of MoS_2/PGS PDs. Reproduced with permission.[18] Copyright 2021, American Chemical Society. d) Synthetic route to obtain a ZnO/Si substrate and e) photoresponse of ZnO/Si PDs. Reproduced with permission.[19] Copyright 2022, The Royal Society of Chemistry. f) Synthetic route of TiO_2/BiOCl heterostructure PDs. Reproduced with permission.[20] Copyright 2018, Wiley-VCH.

and applications of optoelectronic materials in detection. The key figures of merit summarized in **Table 1** are used to evaluate the device performance.

2.1. Traditional Semiconductor Optoelectronic Materials

2.1.1. Group III–V Materials

Currently, Si-based, group III–V compounds and mental oxides are the main optoelectronic materials for industrialization and commercial application. To achieve the better performance, many experiments on element component, structural design, and external field have been done in the lab. As III–V semiconductors, InAs nanowires have high carrier mobility and long mean free path. How to control the surface defect state to meet its optoelectronic application has become a hot issue. Miao et al. reported InAs nanowires near-infrared ray (NIR) PDs with a detection wavelength of up to 1.5 μm (**Figure 2**a).[17] It is noteworthy that different contact modes exhibited extremely distinct results. The Schottky–Ohmic contact showed a responsivity of 5.3×10^3 A W^{-1}, three times greater than the Ohmic–Ohmic contact mode. Under the strong internal electric field derived from Au-cluster, InAs PDs presented dramatically enhanced responsivity compared with the original one (Figure 2b).

© 2023 Wiley-VCH GmbH

23669608, 0, Downloaded from https://onlinelibrary.wiley.com/doi/10.1002/smtd.202300319 by Fudan University, Wiley Online Library on [28/08/2023]. See the Terms and Conditions (https://onlinelibrary.wiley.com/terms-and-conditions) on Wiley Online Library for rules of use; OA articles are governed by the applicable Creative Commons License

Morphological and surface engineering have caught more attention as well. Liu et al. proposed MoS_2 PDs based on patterned GaN substrate (PGS) via the film-transferring method (Figure 2c).[18] Compared with flat GaN substrate, such PGS PDs demonstrated better performance with I_p increasing by five times, noise equivalent power decreasing to 3.88×10^{-13} $WHz^{-1/2}$, and detectivity increasing to 5.6×10^8 Jones.

2.1.2. Transitional Metal Oxides

The unsaturation of transition metal d orbital endows metal oxides with unique properties, resulting in direct or indirect applications in optoelectronic science. The morphologies and structures of metal oxides such as nanosheets, nanorods, nanospheres, and other microstructures are becoming increasingly diverse. As a conventional semiconductor, ZnO with high electron mobility and exciton binding energy has been used in UV detection. Jang et al. presented a direct Si etching transfer method to prepare flexible ZnO nanorods PDs (Figure 2d,e).[19] Such PDs demonstrated excellent flexibility and stability in the static bending test. The on/off ratio and rise/decay times of PDs have reached 431 and 1.08/0.69 s.

In the active layer, once the photogenerated carriers are separated and transferred inefficiently, the recombination will occur and hurt optoelectronic conversion efficiency. Constructing a heterogeneous system is a practical strategy to suppress the recombination of electron–hole pairs. Figure 2f shows a $BiOCl/TiO_2$ heterojunction UV PDs fabricated via anodic oxidation and impregnation.[20] The internal electric field facilitated the separation of carriers and tuned the electron motion. An on/off ratio was reached up to 2.2×10^5, and fast decay speed was 0.81 s. In addition, TiO_2 with nanoporous structures has a large specific surface area, which is suitable for photosensitizers deposition. The energy level structure is favorable for the transportation of photo-generated electrons, so TiO_2 is often used as photoanode for solar cells and photocatalytic devices.[21,22]

2.2. 2D Optoelectronic Materials

2.2.1. Typical 2D Materials: Graphene

Graphene is representative of 2D materials with many excellent physical properties, such as gapless band, ultrafast photocarrier dynamics, and high carrier mobility. Also, the unique planar 2D structure determines the transparency, flexibility, and high mechanical strength. Meanwhile, there are many challenges in the research of graphene-based PDs. Graphene has a zero bandgap structure; its light absorption depends on the fine-structure constant, and the absorption of monolayer graphene is 2.3%. Hence, the limitation of low absorption and large dark current need to be overcome. Hybrid structures, one of the practical solutions, are often exploited in photoelectron devices.[23] To date, many graphene-based hybrid PDs have been reported, including MoS_2/hBN/graphene,[24] hBN/graphene/WSe_2/graphene/hBN,[25] and graphene/$MoTe_2$/graphene heterojunctions.[26] Moreover, creating a tunable p–n junction in a channel by applying a localized field is also an effective way for optoelectronic detection. In the fifth section, we will give several examples of ferroelectrics used as gate insulators to construct the graphene-based homojunctions.

2.2.2. Transition Metal Dichalcogenides

The general formula of transition metal dichalcogenides (TMDs) is MX_2, where M (M = Mo, W) is the transition metal element located at the center of unit cell, X (X = S, Se, Te) is the sulfur group element located at the top and bottom sides, forming a sandwich structure of X–M–X. Owing to the atomic thinness, direct bandgap, and strong photon–matter interaction, 2D TMD semiconductors have become a good candidate for photoelectric detection, especially in the visible range. Hong et al. reported an efficient and scalable method for preparing large-area MoS_2 film.[27] By the electrohydrodynamic-jet printing process, the MoS_2-based PDs were fabricated with two/three-terminal modes (**Figure 3**a). As shown in Figure 3b,c, the higher photosensitivity of 4495% and faster photoresponsivity of 3.78 A W^{-1} were achieved in the three-terminal mode. However, the ultrathin scale of TMDs also increases defects and transfer resistance, resulting in a large noise and reduced photoresponse for PDs. Hence, combining 2D materials and other materials, such as GaN and TiO_2, and even ferroelectrics, has caught more attention to realize the modulation of optical and electric properties. The P(VDF-CTFE) as a ferroelectric gate was integrated into WS_2/Si heterojunction PDs.[28] There are two effects induced by the polarization electric field: 1) widened the range of absorption wavelength; 2) enhanced the sensitivity of lateral photovoltaic effect. Moreover, downward polarization enhanced the hole–electron pairs' separation efficiency and showed greater sensitivity than that of upward polarization mode in various light intensities (Figure 3d). Compared with non-polarized state, the photocurrent was dramatically promoted after giving a ferroelectric field (Figure 3e).

2.3. Perovskites Optoelectronic Materials

2.3.1. All-Inorganic Perovskites

The perovskite structure can be represented by the general formula of ABX_3, where A is rare- or alkaline-earth cation, B is transition metal cation, and X is a halogen or oxygen anion. The A-site ion is surrounded by 12 X ions, and the B-site ion is coordinated with 6 X ions to form an octahedron structure.

In general, all-inorganic perovskites have excellent optical absorption in the visible light range, a broad flat absorption at short wavelength, and strong absorption at edge wavelength. Meanwhile, changing the X component can easily adjust the band gap and optical absorption of all-inorganic halide perovskites. Cao et al. reported $Cs_3Bi_2Br_9/Cs_3BiBr_6$ heterojunction PDs for light communication.[8] The perovskite heterojunction demonstrated the optical characteristic on dual-band photodetection. The PDs have reached a high responsivity of 5.6 mA W^{-1} at 360 nm and a vice-peak responsivity of 0.6 mA W^{-1} at 450 nm. Based on its dual-band photodetection, the output electrical signals were defined according to different current densities, achieving dual-band light communication.

© 2023 Wiley-VCH GmbH

23669608, 0, Downloaded from https://onlinelibrary.wiley.com/doi/10.1002/smtd.202300319 by Fudan University, Wiley Online Library on [28/08/2023]. See the Terms and Conditions (https://onlinelibrary.wiley.com/terms-and-conditions) on Wiley Online Library for rules of use; OA articles are governed by the applicable Creative Commons License

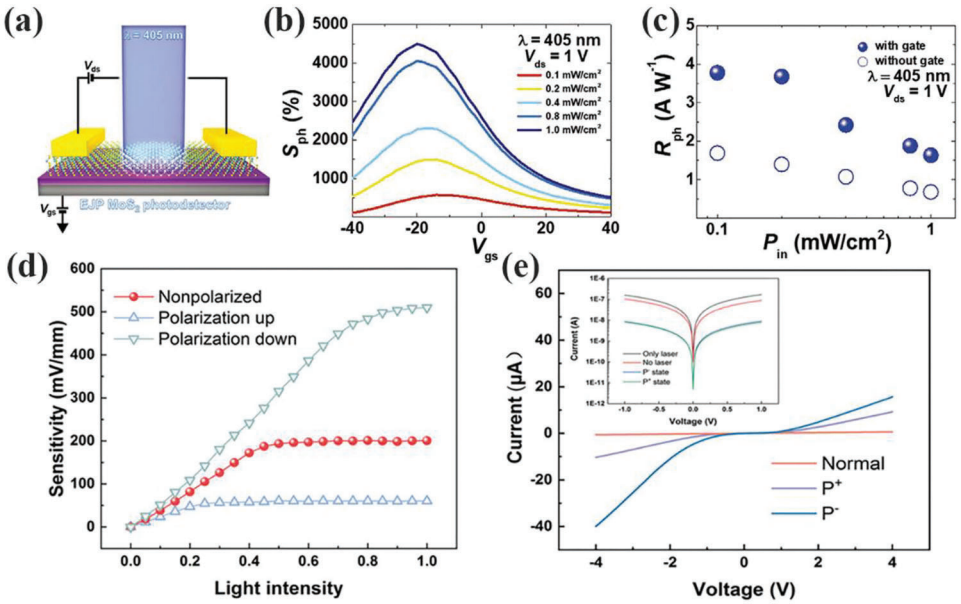

Figure 3. a) Schematic of MoS_2 PDs with three-terminal mode. b) Photosensitivity and c) photoresponsivity of MoS_2 PDs. Reproduced with permission.[27] Copyright 2022, Wiley-VCH. d) The lateral photovoltage sensitivity under different light intensities. e) *I–V* curves of different polarized states. Reproduced with permission.[28] Copyright 2021, Wiley-VCH.

Given the characteristics of ionic crystals, however, all-inorganic perovskite is very easy to decompose and phase change in highly polar solvents or high-temperature environments. Studies have shown that the luminescence of $CsPbBr_3$ nanocrystals can be quenched by more than 80% at 85 °C for 5 min or in water for 3 h.[29] Therefore, poor stability is the main resistance for its application.

2.3.2. Organic–Inorganic Hybrid Perovskites

In organic–inorganic hybrid perovskite, an organic molecule, such as $CH_3NH_3^+$ and $CH_3CH_2NH_3^+$, replace the A component in ABX_3. Compared with all-inorganic perovskites, the diversity of organic components provides opportunities to design new material characteristics. Therefore, organic–inorganic hybrid perovskites have been investigated extensively in optics and electronics.

Hong et al. proposed a facile aqueous floating growth method to synthesize single-crystalline 2D perovskite $BA_2MA_{n-1}Pb_nI_{3n+1}$ (BA is *n*-butylamine, MA is CH_3NH_3).[30] The optoelectronic properties of the $BA_2MA_{n-1}Pb_nI_{3n+1}$ can be adjusted by composition engineering. The PDs based on perovskite with index n = 4 showed a low dark current and a large on/off ratio of 3.5 orders of magnitude. Here, vertically oriented hetero-/homo-junctions stacked via the convenient transfer method exhibited good self-powered characteristics (**Figure 4**a,b).

As a result of the order–disorder transition of organic molecules and/or deformation of inorganic framework, spontaneous polarization was observed in some organic–inorganic hybrid perovskites. Luo et al. constructed the first hybrid ferroelectric perovskite $BA_2MA_2Pb_3Br_{10}$ (BA = $C_4H_9NH_3$, MA = CH_3NH_3) by cooling the supersaturated solution.[31] It should be pointed out that the ferroelectricity was formed by molecular re-orientation and synergic ordering of organic moieties. Such single-crystal PDs demonstrated excellent performance, including ultralow dark current, large on/off ratio, and fast photoresponse (Figure 4c,d). Their work is significant for organic–inorganic hybrid perovskites to be applied in optoelectronic detection. More discussion about the perovskite ferroelectrics will be presented in the following section.

2.4. Organic Optoelectronic Materials

Compared with inorganic semiconductor-based PDs, simple process, large area preparation, and mechanical flexibility are the distinctive advantages of organic materials-based PDs. At present, the organic optoelectronic materials used in PDs mainly include polymer, small molecule, fullerene, and non-fullerene molecules, which are usually used to fabricate devices in the form of planar heterojunction and vertical heterojunction structures. The existing organic materials not only covered the panchromatic detection from UV to NIR but also realized the detection of specific wavelengths via the adjustment of molecules.

Heeger et al. reported polymer-based PDs with a high detectivity of up to 10^{12} Jones and a wide linear dynamic range of more than 100 dB. Further, it is worth noting that a broad spectral response from 300 to 1450 nm was reached with the cooperation of small band-gap semiconducting polymer and fullerene derivative.[33] Similarly, the PDs with broadband photoresponse in 300–1000 nm range were demonstrated by adjusting the proportion of components in active layer.[34] Wang et al. proposed a strategy of polyethylenimine ethoxylated (PEIE)-modified ITO electrode. (Figure 4e,f).[32] Here, the PEIE organic layer with high transparency blocked unnecessary electronic charge injection and reduced dark current, which is a new solution to

© 2023 Wiley-VCH GmbH

23669608, 0, Downloaded from https://onlinelibrary.wiley.com/doi/10.1002/smtd.202300319 by Fudan University, Wiley Online Library on [28/08/2023]. See the Terms and Conditions (https://onlinelibrary.wiley.com/terms-and-conditions) on Wiley Online Library for rules of use; OA articles are governed by the applicable Creative Commons License

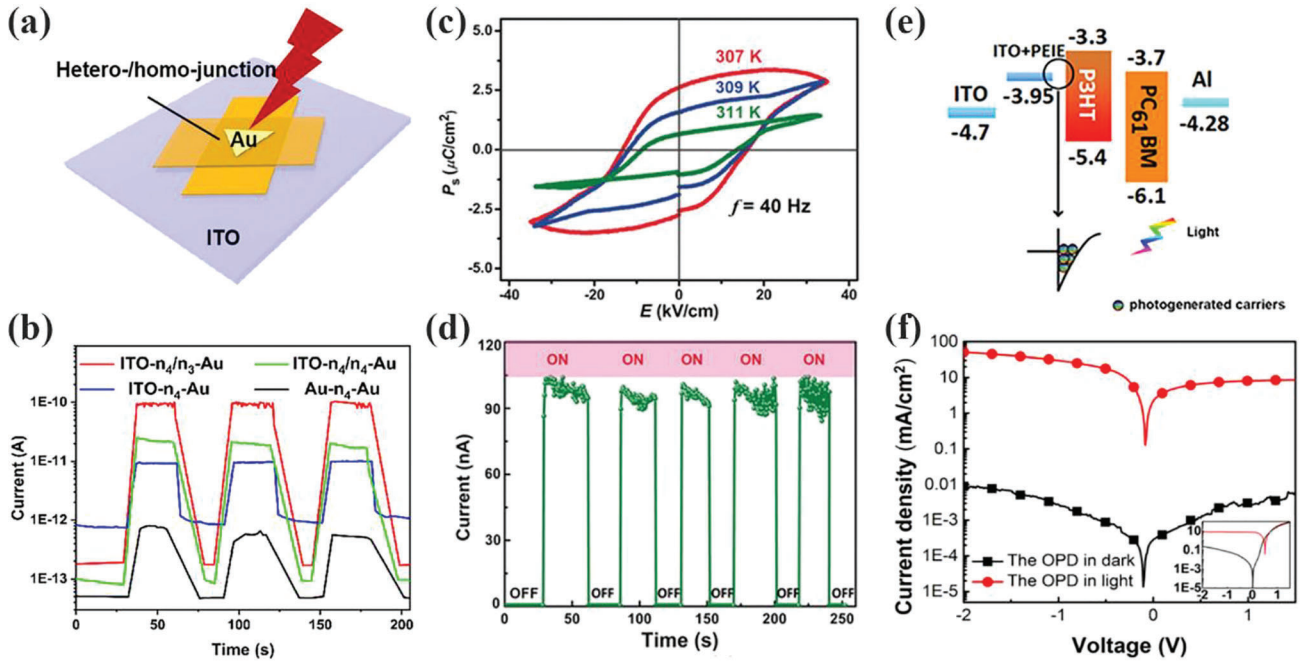

Figure 4. a) Schematic of hetero-/homo-junction PDs. b) *I–t* curves of four different PDs for three cycles. Reproduced with permission.[30] Copyright 2022, American Chemical Society. c) Polarization–electric field hysteresis loops tested at different temperatures. d) *I–t* curves of PDs for five cycles. Reproduced with permission.[31] Copyright 2017, Wiley-VCH. e) The energy level diagram of the PDs. f) *I–V* curves of PDs on ITO-PEIE and ITO (inset), respectively. Reproduced with permission.[32] Copyright 2017, Optical Society of America.

reduce the dark current and different from the previous strategies of manufacturing double-layer or multilayer devices.

With the advances in technology, the requirements for the response speed and detection measurement of PDs will be more stringent. The main challenges faced today are the high dark current, low absorption efficiency, and high cost. However, doping, defect engineering, morphological engineering, device structure design, and other methods no longer fully meet the severe demands of high-performance PDs. A new manipulation way, introducing localized fields in a microscopic space, to suppress background noise and improve carrier separation efficiency will be desirable. The ferroelectric polarization field with non-volatile and rewritable characteristics could realize reversible polarization doping and controllable electrostatic doping, which will be an outstanding candidate.

3. Introduction of Ferroelectric Materials

3.1. Fundamentals of Ferroelectrics

Ferroelectrics are dielectric materials that develop spontaneous polarization in a range of temperatures. The spontaneous polarization could be switched into the opposite direction by applying an external electric field, thus a polarization–electric field (P–E) hysteresis loop. The P–E hysteresis loop is an important characteristic of ferroelectrics. **Figure 5**a exhibits the hysteresis loop of ferroelectrics programmed by an external electric field. The polarization intensity of the ferroelectrics has a non-linear relationship with the applied electric field and presents a hysteresis performance. P_s is the saturated polarization with different polarization directions (points a and b). The remnant polarization (P_r) under zero electric field is at points c and d. The coercive field (E_c) corresponds to randomize aligned dipoles (points e and f). Generally, ferroelectricity exists in a specific temperature range and Curie temperature (T_c) is the temperature of paraelectric–ferroelectric transition. When the temperature is lower than T_c, the phase transition will emerge from the high-symmetry paraelectric phase to the low-symmetry ferroelectric phase. Here, the phase above T_c is designated as high-temperature phase (HTP), and the phase below T_c is designated as low-temperature phase (LTP), respectively. Such ferroelectric characteristics are essential references for designing and applying of ferroelectric materials.

3.2. Perovskite Ferroelectric Materials

3.2.1. Inorganic Perovskite Ferroelectrics

Perovskite ferroelectric materials are the most numerous and widely studied ferroelectrics. Among them, the perovskite oxides are the most studied. Perovskite oxides have a chemical formula of ABO_3, and the X component in ABX_3 is the oxygen atom (Figure 5b). A library of ABO_3 perovskite ferroelectrics contains several typical perovskite oxides, including $PbTiO_3$ (PTO), $BaTiO_3$ (BTO), $PbZr_xTi_{1-x}O_3$ (PZT), $BiFeO_3$ (BFO), and $LiNbO_3$ (LN). As for ferroelectrics, the phase transition phenomenon from paraelectric phase to ferroelectric phase can be classified as displacive type, order–disorder type, and mixed order–disorder and displacive type. PTO has excellent ferroelectric,

© 2023 Wiley-VCH GmbH

23669608, 0, Downloaded from https://onlinelibrary.wiley.com/doi/10.1002/smtd.202300319 by Fudan University, Wiley Online Library on [28/08/2023]. See the Terms and Conditions (https://onlinelibrary.wiley.com/terms-and-conditions) on Wiley Online Library for rules of use; OA articles are governed by the applicable Creative Commons License

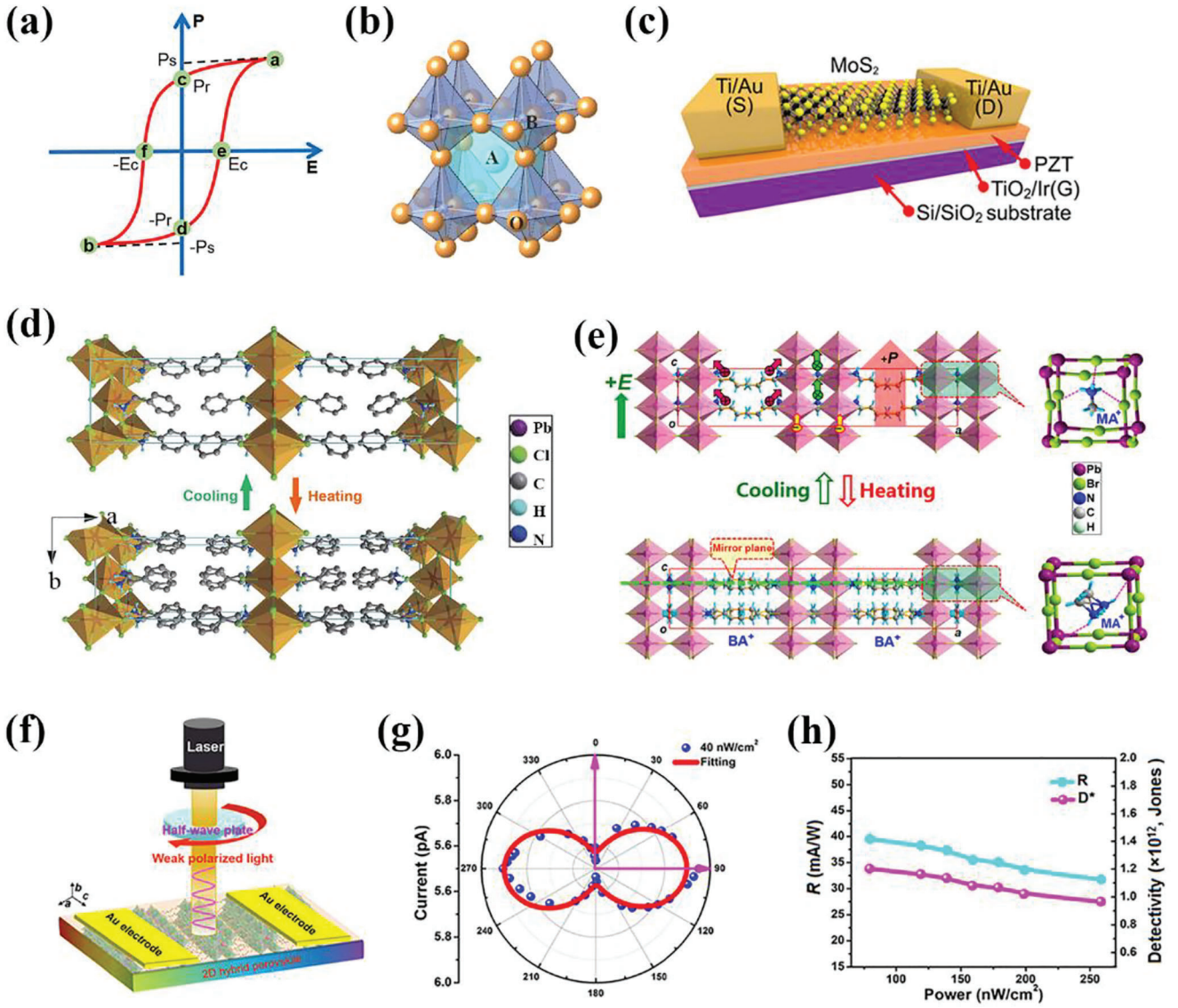

Figure 5. a) The *P–E* hysteresis loop of ferroelectrics. b) The structure of perovskite oxides ABO_3. c) Schematic of a MoS_2/PZT Fe-FET. Reproduced with permission.[35] Copyright 2015, American Chemical Society. d) The crystal structures of $(benzylammonium)_2PbCl_4$ and e) $(BA)_2(MA)Pb_2Br_7$ between the paraelectric and ferroelectric phases. Reproduced with permission.[36] Copyright 2015, Springer Nature. Reproduced with permission.[37] Copyright 2019, American Chemical Society. f) Schematic diagram of polarized light PD. g) Polar plot of the normalized angle-resolved photocurrent. h) Responsivity and detectivity versus incident-light density. Reproduced with permission.[38] Copyright 2020, Science China Press.

piezoelectric, and pyroelectric properties. PTO is displacive type phase transition with a high T_c of ≈ 763 K. When the temperature is lower than T_c, both Ti^{4+} and O^{2-} ions are displaced upward in the direction [001], while the displacement of O^{2-} ion is greater than that of Ti^{4+} ion, resulting in a net dipole moment. Hence, PTO undergoes a phase transition from the cubic paraelectric phase ($Pm\bar{3}m$) to the tetragonal ferroelectric phase ($P4mm$). It can be seen that the displacive type spontaneous polarization arises from the lattice distortion caused by the displacement of the atoms. Another displacive type ferroelectric is BTO, whose Curie point is 393 K. At LTP, Ti^{4+} has an off-center displacement along the [001] direction, leading to spontaneous polarization, thus a phase transition from the cubic paraelectric phase ($Pm\bar{3}m$) to the tetragonal ferroelectric phase ($P4mm$).

Regarding the applications of perovskite oxide ferroelectrics, Su et al. reported integrated PDs based on TiO_2 (TO) film and BTO film. The high crystalline interface and spontaneous polarization are beneficial to the separation of carriers. A high responsivity of BTO/mTO PDs was measured up to 8.53 mA W^{-1} under 310 nm, and the on/off ratio increased up to 680, which is 17 times than that of original TO PD.[39] Also, PZT was used as a gate dielectric in the MoS_2/PZT Fe-FET structure. The interaction of polarization effect and interfacial phenomena were discussed by Sinitskii et al., demonstrating the advantages of MoS_2/PZT structure on random-access memory (RAM) devices (Figure 5c).[35]

Compared with perovskite oxides, all-inorganic halide perovskites have received less attention in the ferroelectric field.

© 2023 Wiley-VCH GmbH

23669608, 0, Downloaded from https://onlinelibrary.wiley.com/doi/10.1002/smtd.202300319 by Fudan University, Wiley Online Library on [28/08/2023]. See the Terms and Conditions (https://onlinelibrary.wiley.com/terms-and-conditions) on Wiley Online Library for rules of use; OA articles are governed by the applicable Creative Commons License

Halide perovskites have the same crystal structure as perovskite oxides in which the oxygen ion is replaced by a halide ion (e.g., Cl^-, Br^-, or I^-). To date, there are a few researches on the ferroelectricity of all-inorganic halide perovskites. Similar to the abovementioned perovskite oxides, some studies have shown that the ferroelectricity of all-inorganic halide perovskites is induced by the symmetry breaking of the crystal structure. For example, the reversible transition in $CsPbBr_3$ quantum dots is driven by the offset of C_s^+ from the center of unit cell and the distortion and tilting of $[PbBr_6]^{4-}$ octahedron.[40] Also, Smith et al. studied the origin of ferroelectricity in $CsPbF_3$ by the first-principles calculation.[41] The results revealed that the ferroelectricity of $CsPbF_3$ is due to the Pb^{2+} ion pair.

3.2.2. Organic–Inorganic Hybrid Perovskite Ferroelectrics

By contrast, the organic–inorganic hybrid perovskites where A component in ABX_3 is an organic molecule have attracted more attention. Organic–inorganic hybrid perovskites are composed of inorganic octahedra as the skeleton and organic functional groups as the flesh, forming a network by hydrogen bonds and van der Waals forces. Xiong's team summarized the design and synthesis experiences of ferroelectric compounds based on the Neumann's principle and the Curie symmetry principle, and further proposed the "quasi-spherical theory" to better design multiaxial molecular ferroelectrics.[42] The diversity of organic components makes the hybrid structures more flexibility and tunability, so organic–inorganic hybrid perovskites have been extensively investigated in the fields of optics and electronics, especially in high-performance photovoltaics. Meanwhile, they also show excellent ferroelectric and piezoelectric properties, which are not inferior to conventional inorganic compounds.

Generally, the ferroelectricity of most organic–inorganic hybrid perovskites is due to the mixed order–disorder and displacive type mechanism, that the coupling of organic cations order–disorder transition and deformation of inorganic framework causes the spontaneous polarization. Taking $(benzylammonium)_2PbCl_4$ as an example, it has a superior spontaneous polarization of P_s = 13 μC cm^{-2}, and a high T_c of 438 K, which suggests good ferroelectric properties.[36] As shown in Figure 5d, the inorganic layers are interlaced with the organic layers along the *a*-axis. $PbCl_6$ octahedra combined to construct inorganic layers by corner-sharing, and benzylammonium cations establish a link with inorganic layers by N–H···Cl hydrogen bonds. At HTP, it is centrosymmetric, while the organic benzylammonium cations located at the twofold screw axis perpendicular to the *bc* plane are in a highly dynamic disordered orientation. At LTP, all organic cations present an ordered state where the C–N bonds are oriented along the *c*-axis, resulting in a spontaneous polarization along the *c*-axis.[43]

In the case of $(BA)_2(MA)Pb_2Br_7$ (MA is $CH_3NH_3^+$, BA is n-butylammonium) with a P_s of 3.6 μC cm^{-2}, $MAPbBr_3$ is used as a skeleton, BA^+ cations as the flesh are chemically embedded into the skeleton (Figure 5e).[37] The organic and inorganic layers are arranged alternately to form a ⟨100⟩ oriented 2D perovskite ferroelectric. At LTP (T_c = 352 K), the MA^+ cations and BA^+ organic cations are re-ordered, leading the displaced positive charge, while a distorted octahedron causes the negative charge to shift in the opposite direction. Thus, the separation of positive and negative charges results in net dipole moments and spontaneous polarization. At HTP, the $PbBr_6$ octahedra are highly symmetric, while the organic components become disordered and mirror-symmetric, so the dipole moments were canceled out and the macroscopic polarization disappears.[44] This paraelectric–ferroelectric phase transition showed the characteristics of mixed order–disorder and displacive type.

Although the 2D organic–inorganic perovskite ferroelectrics have some shortcomings such as impurities and structure defects, the natural quantum-well structure and excellent physical properties (high carrier transport, structural diversity, etc.) provide great advantages for exploring high-performance photoferroelectrics and some work have been done in polarized light detection, X-ray detection, and self-powered photodetection. As shown in Figure 5f–h, Sun et al. reported polarized light PDs assembled on single-crystal ferroelectric $BA_2CsPb_2Br_7$.[38] Owing to the unique bilayer structure, 2D $BA_2CsPb_2Br_7$ exhibited a strong electrical and optical anisotropy. Such PDs present a high responsivity (39.5 mA W^{-1}) and detectivity (1.2 × 10^{12} Jones) under a low detectable limit (40 nW cm^{-2}). Also, Luo et al. reported a passive detection of X-ray photons based on a quasi-2D hybrid ferroelectric $(CH_3OC_3H_9N)_2CsPb_2Br_7$. The PDs demonstrated a sensitivity up to 410 μC Gy^{-1} cm^{-2} at zero bias.[45] These studies revealed the great potential of organic–inorganic hybrid ferroelectrics for photodetection. To date, compared with all-inorganic perovskite ferroelectrics, organic–inorganic hybrid ferroelectrics are still in their infancy. With further research on the mechanism of hybrid perovskite ferroelectrics, their applications will be further explored.

3.3. Fluorite-Structure Ferroelectric Materials

Due to the critical size effect, the ferroelectricity will be suppressed in ultra-thin ferroelectrics. First-principles calculations predicted that six-unit cells are the critical thickness in perovskite ferroelectrics, which does not satisfy the modern semiconductor process.[46,47] Since the ferroelectricity of Si-doped HfO_2 films was first discovered in 2011 (**Figure 6**a),[48] emerging fluorite-structure ferroelectrics, such as HfO_2, ZrO_2, and mixed $Hf_{1-x}Zr_xO_2$ (HZO, x = 0–1), exhibited excellent ferroelectricity at nanoscale and the thickness of ferroelectric film is continuously reduced down to ≈ 1 nm (Figure 6b,c).[46] From a crystallographic perspective, the orthorhombic phase and rhombohedral phase are non-centrosymmetric phases, which are suggested as the origin of the ferroelectric properties in fluorite-structure ferroelectrics.[49–51] Meanwhile, the formation of ferroelectric phase depends both on thermodynamic and kinetic factors in the preparation process, such as doping, oxygen content, stress, and surface/interfacial energy.[52–55]

As the scaling issues were resolved, HfO_2 with a large dielectric constant (20–25) and wide band gap (5.5 eV) was further combined with other ultrathin fundamental materials to reach the miniaturization of photodetection, Fe-FET, and ferroelectric memory devices. For example, Salahuddin et al. fabricated negative capacitance FETs with a 1.8 nm Zr-doped HfO_2 gate layer.[56]

© 2023 Wiley-VCH GmbH

23669608, 0, Downloaded from https://onlinelibrary.wiley.com/doi/10.1002/smtd.202300319 by Fudan University, Wiley Online Library on [28/08/2023]. See the Terms and Conditions (https://onlinelibrary.wiley.com/terms-and-conditions) on Wiley Online Library for rules of use; OA articles are governed by the applicable Creative Commons License

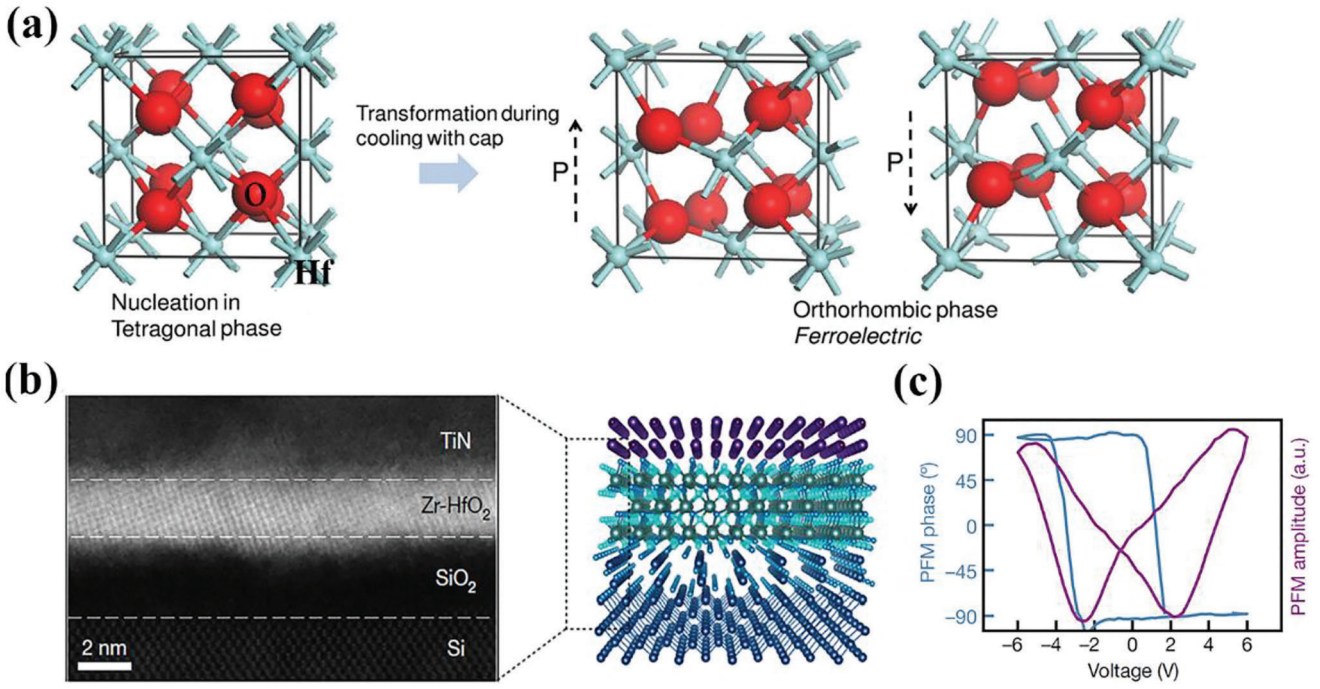

Figure 6. a) The tetragonal phase and ferroelectric phase of HfO_2. Reproduced with permission.[48] Copyright 2011, American Institute of Physics. b) The heterostructure of ultrathin ferroelectric HZO layer deposited on Si/SiO_2. c) Phase and amplitude switching spectroscopy loops for a ten cycle HZO film. Reproduced with permission.[46] Copyright 2020, Springer Nature.

3.4. 2D Ferroelectric Materials

Since the successful isolation of graphene in 2004, 2D layered materials, including TMDs, hexagonal boron nitride (h-BN), black phosphorus, and MXene, have been discovered driven by their novel electrical, optical, and mechanical properties. Particularly, the 2D ferroelectrics with non-centrosymmetry structures have great potential in electromechanical and optoelectronic systems. So far, various 2D layered ferroelectrics have been experimentally demonstrated, such as group IV monochalcogenides, d1T-$MoTe_2$, α-In_2Se_3, and $CuInP_2S_6$ (CIPS). The spontaneous polarization of intrinsic 2D ferroelectrics, attributed to space inversion symmetry breaking and/or offset from the center of negative/positive charges, can be divided into three types: out-of-plane (OOP) polarization, in-plane (IP) polarization, and intercorrelated polarization (both OOP and IP polarizations). The following section will discuss the three 2D ferroelectrics with different polarization types.

3.4.1. Typical 2D OOP Ferroelectric: CIPS

Layered CIPS is a typical representative of OOP ferroelectrics. As shown in **Figure 7**a, the crystal structure of CIPS is that S atoms are linked by covalent bonds to form a framework in which the octahedral cavities are filled with Cu^+, In^{3+}, and P–P pairs trigonal modes. For 2D layered CIPS, the paraelectric–ferroelectric phase transition occurs at $T_c \approx$ 320 K. The ordering of the Cu ions in two off-center sites in the crystal lattice leads to symmetry breaking in the vertical layer plane direction and OOP ferroelectricity.[57–59] With advances in thin film preparation, ferroelectricity has been detected in ultrathin films several nanometers thick. The ferroelectricity in CIPS samples is also given serious attention. In 2015, Belianinov et al. showed the ferroelectric polarization of 2D CIPS flakes down to 50 nm by characterizing domain structures, switchable polarization, and hysteresis loops.[60] In 2016, Chyasnavichyusr et al. discussed the critical size effect of 2D ferroelectric CIPS flakes at a thickness of ≈10 nm.[61] Subsequently, Liu et al. studied the atomic force microscopy (AFM) and piezo-response microscopy (PFM) phase images of ultrathin CIPS flakes, confirming the switchable polarization in CIPS down to ≈4 nm at room temperature (Figure 7b).[57] These thickness limit studies of 2D layered CIPS are contributing to new physical properties of 2D material systems as well as new insights into van der Waals heterostructure devices.

3.4.2. Typical 2D IP Ferroelectric: SnTe

As mentioned above, polarization in conventional ultrathin ferroelectrics strongly depends on the thickness of samples due to the depolarization effect and interface/surface polarization pinning.[57] Atomic-thick SnTe, down to a 1-unit cell, was reported as IP polarization ferroelectric in 2016.[14] At room temperature, SnTe is a cubic rock-salt structure in which Sn and Te atoms are arranged alternately via Sn–Te covalent bonds in [100], [010], and [001] directions (Figure 7c).[64] At T_c = 98 K, the SnTe bulk undergoes a cubic–rhombohedral phase transition, which is induced by the lattice distortion and the band-bending at the edge of SnTe islands (Figure 7e).[14] Interestingly, as the thickness reduced down to the 1-unit cell, the T_c of SnTe reaches 270 K,

© 2023 Wiley-VCH GmbH

23669608, 0, Downloaded from https://onlinelibrary.wiley.com/doi/10.1002/smtd.202300319 by Fudan University, Wiley Online Library on [28/08/2023]. See the Terms and Conditions (https://onlinelibrary.wiley.com/terms-and-conditions) on Wiley Online Library for rules of use; OA articles are governed by the applicable Creative Commons License

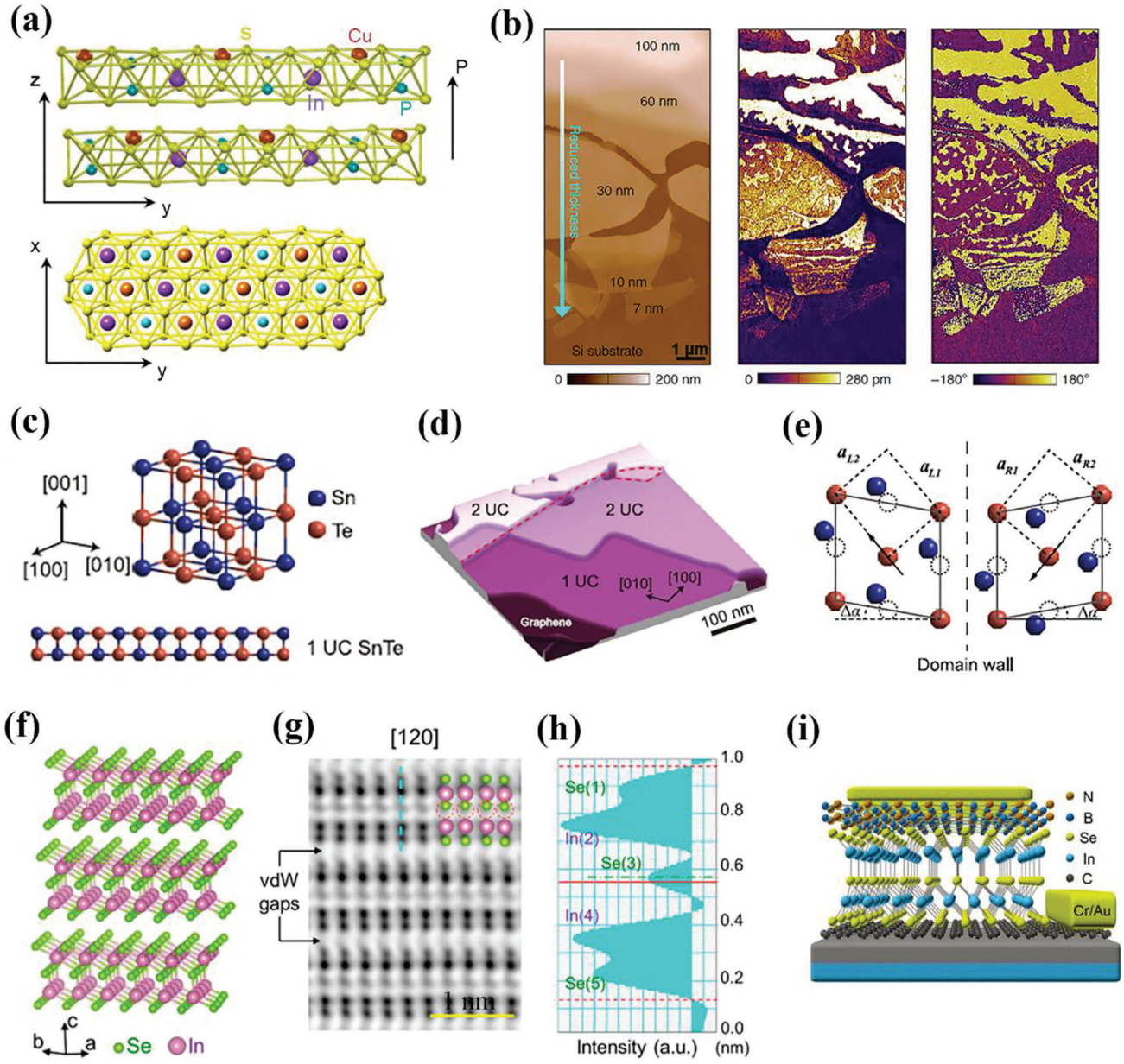

Figure 7. a) The crystal structure of CIPS. b) AFM topography, PFM amplitude, and PFM phase of CIPS nanoflakes ranging from 100 to 7 nm thickness. Reproduced with permission.[57] Copyright 2016, Springer Nature. c) The crystal structure of SnTe. d) Typical STM topography image of SnTe film. e) Schematic of the lattice distortion and atom displacement of SnTe. Reproduced with permission.[14] Copyright 2016, AAAS. f) Atomic structure of layered In_2Se_3 nanoflakes. g) Cross-sectional STEM image of In_2Se_3 nanoflake along the [120] direction. h) Intensity profile along the blue dashed line in (g). Reproduced with permission.[62] Copyright 2017, American Chemical Society. i) Schematic of h-BN/α-In_2Se_3/graphene FTJ. Reproduced with permission.[63] Copyright 2022, Wiley-VCH.

possibly due to the interplay between hybridization interaction and Pauli repulsion based on first-principles calculations.[14,65]

Owing to the small size, the ultrathin SeTe-based FTJs structure for RAM was prepared and achieved an on/off ratio of 3000.[14] Furthermore, Slawinska et al. predicted the intrinsic persistent spin helix (PSH) and spin Hall effect (SHE) in ultrathin SnTe via first-principles calculations, and an all-in-one spin transistor was fabricated based on the compositive effect of PSH and SHE, showing its great potential in tunable spintronics devices.[66,67] Apart from SnTe, IP polarization ferroelectrics were applied in FTJs (SnSe),[68] ferroelectric diodes (GeS),[69] and van der Waals heterojunctions (GeSe).[70,71]

3.4.3. Typical 2D OOP-IP Ferroelectric: α-In_2Se_3

In addition to the OOP and IP polarization described above, 2D ferroelectrics possess a third polarization type of mixed OOP

© 2023 Wiley-VCH GmbH

23669608, 0, Downloaded from https://onlinelibrary.wiley.com/doi/10.1002/smtd.202300319 by Fudan University, Wiley Online Library on [28/08/2023]. See the Terms and Conditions (https://onlinelibrary.wiley.com/terms-and-conditions) on Wiley Online Library for rules of use; OA articles are governed by the applicable Creative Commons License

and IP polarizations. α-In_2Se_3 is a typical representative of OOP-IP intercorrelated ferroelectrics, and its ferroelectricity with reversible spontaneous polarization was first predicted by first-principles calculations in 2017.[72] Subsequently, the layered α-In_2Se_3 nanoflakes were successfully synthesized and ferroelectricity with both OOP and IP polarization was confirmed.[62,73] As shown in Figure 7f–h, a monolayer α-In_2Se_3 contains five single-element atomic layers. The atoms are linked together by covalent bonds and stacked in order of Se–In–Se–In–Se. The Se atoms in the outer surface layers reside on the vacancies of the neighboring In atomic layers, while the Se atoms in the middle layer are coordinated with the four In atoms in the adjacent layers asymmetrically, with one side connected to an In–Se bond and the other side to three In–Se bonds. The middle Se layer is shifted toward neighboring In layers asymmetrically, breaking the symmetry of crystal structure and leading to OOP ferroelectric polarization.[74] Meanwhile, owing to the lateral movement of middle Se atomic layer, IP ferroelectric polarization exists in α-In_2Se_3 nanoflakes as well.[73]

Benefiting from appropriate bandgap ($\approx$ 1.39 eV), and stable ferroelectricity at ultrathin scale, multiple device types based on 2D α-In_2Se_3 have been reported.[73,75] Graphene/α-In_2Se_3 FeFET demonstrated a non-volatile memory effect, in which the conductance of graphene as conducting channel was modulated via switching polarization of 2D α-In_2Se_3 ferroelectric as a top-gate dielectric.[76] Figure 7i displays the device structure of FTJs based on h-BN/α-In_2Se_3/multilayer graphene van der Waals heterojunction. By introducing α-In_2Se_3 as the tunneling dielectric, such 2D van der Waals FTJs present high thermal stability, reliable cyclic endurance, and a large on/off ratio of 10^4.[63]

3.5. Ferroelectric Organic Polymers

In addition to inorganic ferroelectric materials, organic ferroelectric materials, due to their flexibility, stretchability, physical stability, and large-scale preparation, are often employed for implantable biomedical, flexible wearable, and portable electronic devices. At present, organic ferroelectric polymers mainly include PVDF and its copolymers, odd nylons, polyurethanes, and polyureas. In particular, PVDF and its copolymers are the most popular ferroelectric polymers developed in the last decade.

3.5.1. Molecular Structure and Polymorphs of PVDF

In the 1970s, research on PVDF developed rapidly. The piezoelectricity and pyroelectricity were demonstrated successively,[77,78] and then the axial re-orientation electric poling was measured by X-ray diffraction.[79] Finally, the non-linearity and the hysteresis phenomena under a high electric field were observed by Furukawa and coworkers.[80] PVDF is based on the $-CH_2-CF_2-$ vinylidene (VDF) monomer and divided into four polymorphs (α, β, δ, and γ) according to the different molecular chain conformations (**Figure 8**a). Among the four polymorphs, α and β phases are more common types. The α-phase PVDF has stable thermodynamic characteristics and is often used as a precursor to prepare other PVDF phases. Since the trans (T) and gauche (G) conformations are arranged alternately in a molecular chain of α-phase PVDF, the dipole moments of the neighboring electric dipoles are canceled out due to the opposite direction, that is, it is a non-ferroelectric. In contrast, the β phase has a unit cell consisting of two all-trans conformation chains and a high polarization. As shown in Figure 8a, the molecular chain of β phase crystal is jagged, and the dipole moment of each repeating unit is perpendicular to the molecular chain axis, that is, all dipole moment has the same polarization orientation, leading to a strong molecular polarization of β phase PVDF.[81] Usually, the preparation of pure PVDF is carried out via solution casting or melt-solidification methods. However, pure PVDF is non-polar and paraelectric under ambient conditions, which requires further processing to generate ferroelectricity. The crystalline PVDF phase can be transformed under different treatment conditions (e.g., mechanical stretching and annealing).[9] As illustrated in Figure 8c, α phase spherulites were converted into ferroelectric β phase PVDF films by uniaxial stretching.[82]

3.5.2. PVDF Copolymers

To simplify the additional process, the second monomer molecules such as trifluoroethylene (TrFE) and tetrafluoroetgylene (TFE) are often introduced into PVDF, to obtain a copolymer (such as P(VDF-TrFE) and P(VDF-TFE)) with better stability and superior ferroelectric properties under ambient conditions.[86] P(VDF-TrFE) has a saturated polarization of P_s = 100 mC m^{-1}, and its Curie point decreases with increasing proportion (20–50 mol%) of TrFE monomer. Hence, the phase transition temperature of P(VDF-TrFE) can be changed by adjusting the content of the second monomer of TrFE.[87]

Active research on the synergistic combination of PVDF-based ferroelectric polymers with other optoelectronic functional materials for the facile reconfigurable customization of optoelectronic devices has gained increasing interest. The organic polymer ferroelectric of P(VDF-TrFE) as the gate dielectric and multilayer MoS_2 as a channel were exploited to build up NIR PDs (Figure 8d–f).[85] The P_r of P(VDF-TrFE) offers an ultra-high local electrostatic field of $\approx 10^{9}$ V m^{-1}, which could suppress the dark current of the MoS_2 channel effectively. Such PDs exhibited excellent optoelectronic properties with a high detectivity of 2.2×10^{12} Jones and photo-responsivity up to 2570 A W^{-1}. The polarization of P(VDF-TrFE) can be controlled via the scanning probe/gate bias to define carrier injection and achieve p-type or n-type doping in the active layer.[88,89] According to this, Wang et al. proposed a reconfigurable P(VDF-TrFE)/$MoTe_2$ photoelectric detectors.[1] Similar designs have been reported in other ferroelectric-semiconductor hybrid systems, such as P(VDF-TrFE)/GdS,[90] P(VDF-TrFE)/InP,[91] and PVDF/$CsPbI_3$.[92]

4. Ferroelectric Field Manipulation for Photodetection

Based on programmed ferroelectric polarization, ferroelectric-integrated optoelectronic systems open extensive perspectives for high-performance photodetection. In this section, the modulation effects of ferroelectric polarization field on PDs were discussed. Particular attention was paid to the modulation of ferroelectric field and the interaction between ferroelectrics and semiconductors in ferroelectric–optoelectronic systems.

© 2023 Wiley-VCH GmbH

23669608, 0, Downloaded from https://onlinelibrary.wiley.com/doi/10.1002/smtd.202300319 by Fudan University, Wiley Online Library on [28/08/2023]. See the Terms and Conditions (https://onlinelibrary.wiley.com/terms-and-conditions) on Wiley Online Library for rules of use; OA articles are governed by the applicable Creative Commons License

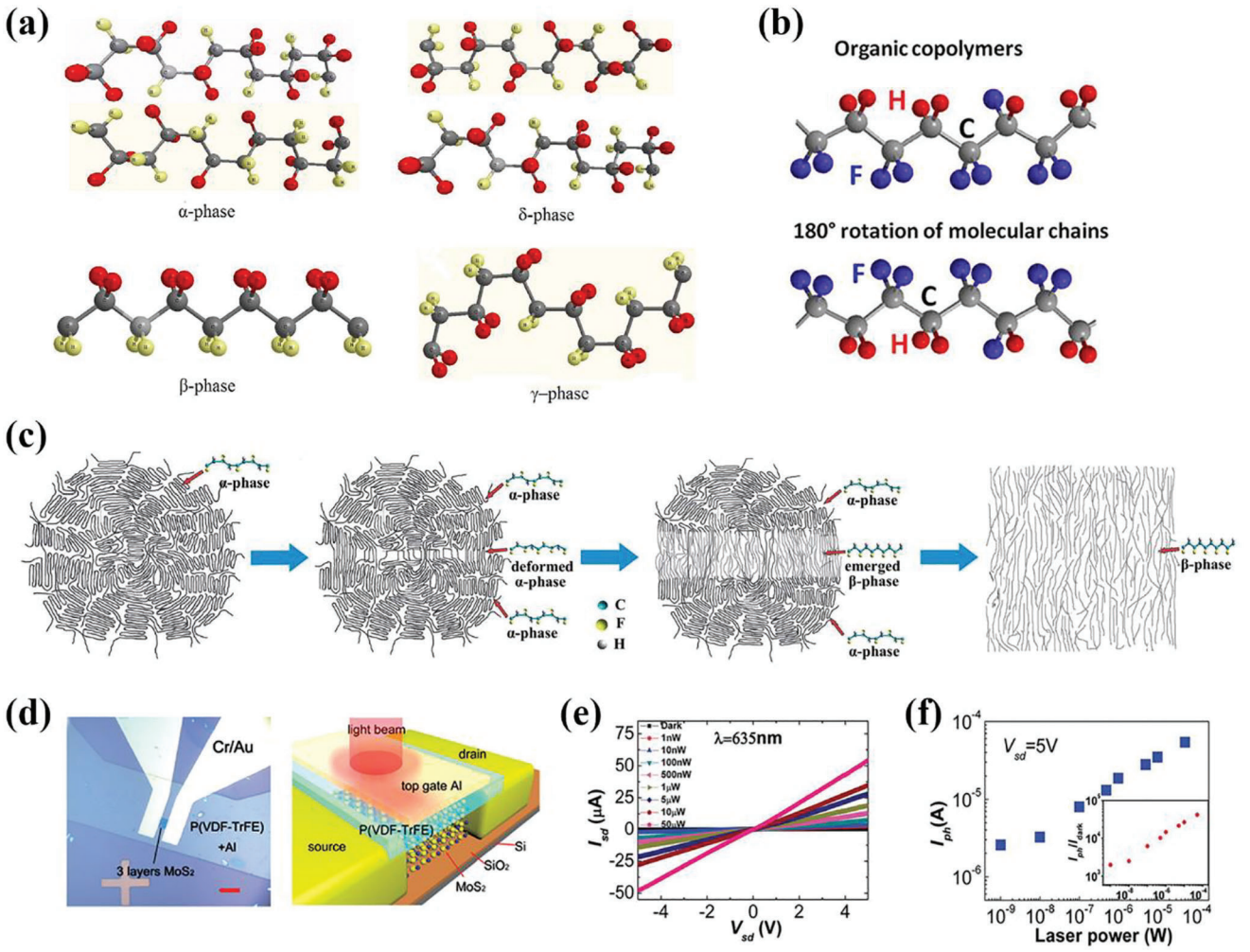

Figure 8. a) The four polymorphs of PVDF. Reproduced with permission.[83] Copyright 2017, IOP Publishing. b) Schematic of molecular structure and polarization switching of P(VDF-TrFE) polymer. Reproduced with permission.[84] Copyright 2014, Springer Nature. c) The transition process of PVDF α-phase to β-phase by mechanical stretching. Reproduced with permission.[82] Copyright 2014, The Royal Society of Chemistry. d) Optical image and schematic of the MoS_2 PD. e) Drain–source characteristic of the PDs. f) Dependence of photocurrent on illumination powers. Reproduced with permission.[85] Copyright 2015, Wiley-VCH.

4.1. Modulation of Energy Band Structures

In nanometer scales, the ferroelectrics were intuitively combined with semiconductors to form the asymmetric band structure; thus the band bending at interface can be manipulated. In the Nb:STO/BFO/graphene hybrid system (**Figure 9**a), holes as the main carriers are accumulated at the interface with a polarization direction toward Nb:STO in ferroelectric film, causing the reduced depletion width at BFO/Nb:STO interface and wider contact barrier at the BFO/graphene interface.[93] Conversely, the electrons are accumulated at the interface under the effect of an opposite polarization field, leading to an opposite trend in the two interfaces. The broadened depletion region and higher recombination barrier were constructed, which prolongs the carrier lifetime and improves the optoelectronic response of PDs.[94] The heterojunction structure PDs based on ferroelectric V-doped ZnO nanosheets and Si film were investigated by Li et al.[95] With an applied bias, a built-in electric field was constructed in ferroelectric layer, accelerating the separation of photogenerated carriers. The holes and electrons are accumulated and depleted at the interface of VZnO/Si, respectively, resulting in the energy band bending upward (Figure 9b). These studies showed that the ferroelectric field can modulate the charge distribution and the band bending at the interface between ferroelectrics and semiconductors and also demonstrated the feasibility of direct manipulation on the energy band at the junction interface by ferroelectricity.

Previous report has demonstrated that ultra-strong ferroelectric local fields can induce change in the bond length and bond angle of low-dimensional crystals, thereby altering the bandgap of optoelectronic materials.[85] In the case of P(VDF-TrFE)/MoS_2 PDs, the response wavelength of the MoS_2 was extended from 850 to 1550 nm under a strong ferroelectric local field. Furthermore, the PL peak of the MoS_2 device driven by upward polarization shifted from 678.46 to 687.26 nm, indicating a decrease in bandgap compared to that of a fresh MoS_2 flake.

© 2023 Wiley-VCH GmbH

23669608, 0, Downloaded from https://onlinelibrary.wiley.com/doi/10.1002/smtd.202300319 by Fudan University, Wiley Online Library on [28/08/2023]. See the Terms and Conditions (https://onlinelibrary.wiley.com/terms-and-conditions) on Wiley Online Library for rules of use; OA articles are governed by the applicable Creative Commons License

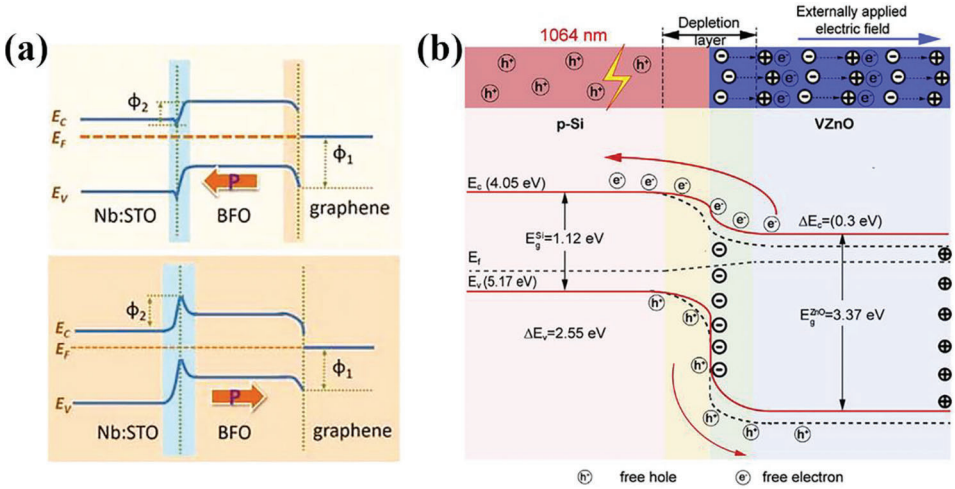

Figure 9. a) The energy band diagrams of the Nb:STO/BFO/graphene heterojunction. Reproduced with permission.[93] Copyright 2018, The Royal Society of Chemistry. b) The energy band diagram of the VZnO/Si heterojunction. Reproduced with permission.[95] Copyright 2019, Elsevier.

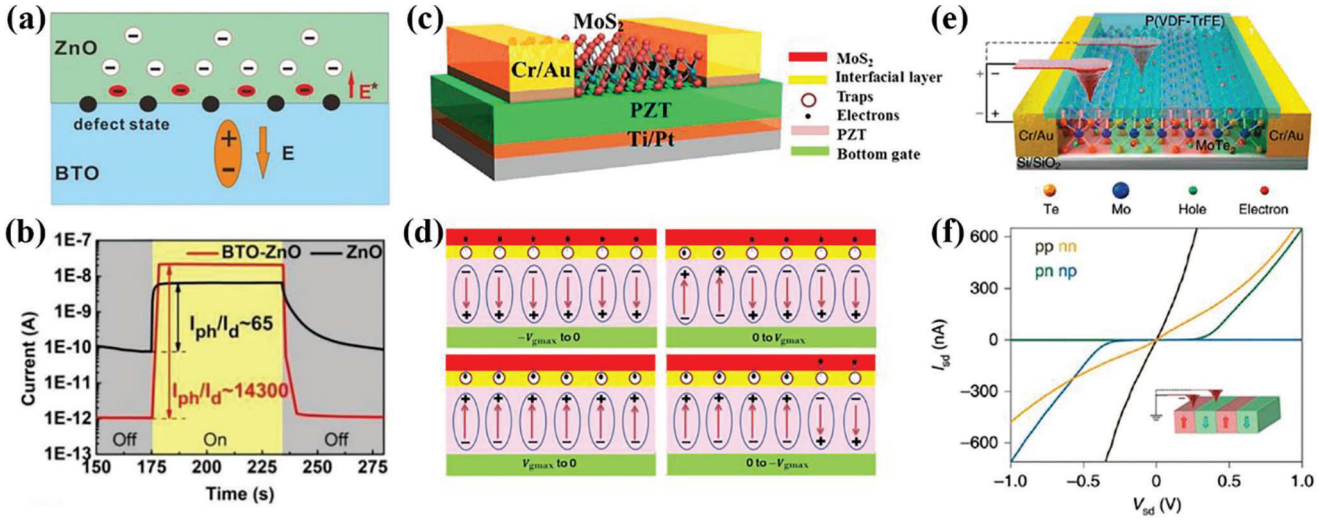

Figure 10. a) Schematic of the electric field in bilayer film. b) The *I–t* curves of PDs for a single period. Reproduced with permission.[98] Copyright 2020, Wiley-VCH. c) The ferroelectric/semiconductor heterojunction system of MoS_2/PZT and d) the mechanism of charge trapping and de-trapping controlled by ferroelectric polarization. Reproduced with permission.[99] Copyright 2016, IOP Publishing. e) The FET structure of $MoTe_2$/P(VDF-TrFE). f) The I_{ds}–V_{ds} curves of different homojunction types. Reproduced with permission.[1] Copyright 2020, Springer Nature.

These findings provide the possibility to extend their detection waveband through energy band engineering.

4.2. Modulation of Carrier Motion by Ferroelectric Field

It has been reported that spontaneous polarization can also be controlled by chemical induction and interface engineering.[96,97] Such ferroelectrics are combined with semiconductors to form the layered heterojunction PDs, whose intrinsic spontaneous polarization modulates the distribution and migration of carriers. For BTO/ZnO layered structure (**Figure 10**a,b), the electron concentration in ZnO film was rearranged under the BTO ferroelectric field. By introducing BTO films, ZnO-based PDs reached a lower dark current and ultra-high on/off ratio of 14 300.[98] This type of polarization modulation is rarely reported. Generally, the construction of a ferroelectric polarization field is facilitated by an external electric field.

In the typical FET-type PDs, ferroelectrics are employed as gate to control charge migration (e.g., suppressing dark current) through the synchronous polarization field programmed by gate bias. As shown in Figure 10c,d, the gating effect on hysteresis behavior in MoS_2/PZT FETs was presented by applying a ferroelectric field.[99] Due to the polarization reversal of the PZT film, the charges in the semiconductor layer were trapped (de-trapped), resulting in a clockwise hysteresis loop. Here, the hysteresis modulation in a ferroelectric/semiconductor system is based on the built-in field in the ferroelectric layer. Additionally, the P(VDF-TrFE) was combined with layered $MoTe_2$-based PDs to

© 2023 Wiley-VCH GmbH

23669608, 0, Downloaded from https://onlinelibrary.wiley.com/doi/10.1002/smtd.202300319 by Fudan University, Wiley Online Library on [28/08/2023]. See the Terms and Conditions (https://onlinelibrary.wiley.com/terms-and-conditions) on Wiley Online Library for rules of use; OA articles are governed by the applicable Creative Commons License

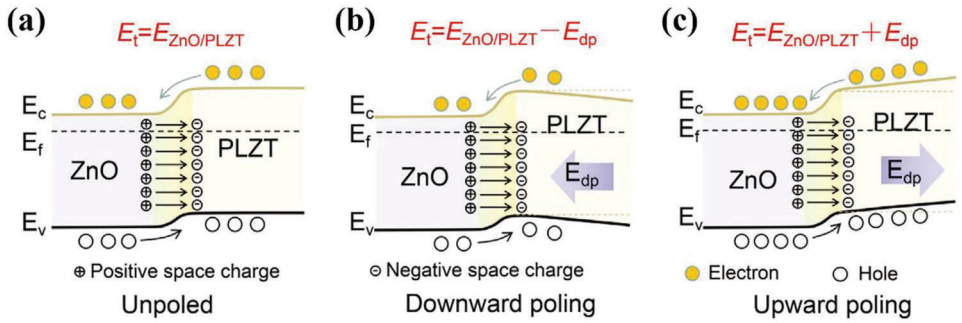

Figure 11. Schematic diagram of the Au/ZnO/PLZT/FTO heterojunctions under a) unpoled, b) downward poling, and c) upward poling states. Reproduced with permission.[102] Copyright 2021, Wiley-VCH.

manipulate the electrical properties of the semiconducting channel (Figure 10e,f). The ferroelectric polarization field programmed by the PFM technique has achieved non-volatile electrostatic doping (p-type or n-type) by establishing a local electrostatic field. Hence, the reversal of ferroelectric field causes periodic polarization domains and constructs the tuned p–n junctions in the channel. Moreover, due to the reversible characteristics, electrostatic doping can be rewritten.[1]

4.3. Synergistic Effect of Ferroelectric Field and Built-In Electric Field

The heterojunction is a classical structure with simple construction and wide application. Regarding photodetection, the separation and transport of photogenerated electron–hole pairs can be accelerated via the built-in electric field in heterojunction. Meanwhile, the diffusion and trapping of carriers also decrease in a dark environment. Therefore, the integration of ferroelectrics into heterojunction systems via structural design may be a new strategy to achieve better detection performance.[100,101] Currently, the main ferroelectrics-integrated heterojunction structures are ferroelectric/semiconductor heterojunction and ferroelectric/metal Schottky junction. In the $ZnO/Pb_{0.95}La_{0.05}Zr_{0.54}Ti_{0.46}O_3$ (PLZT) system, self-powered ZnO/PLZT PDs with II-type heterojunction were manipulated by switching the polarization states.[102] Under the synergistic effect of the ferroelectric depolarization electric field (E_{dp}) and built-in electric field ($E_{ZnO/PLZT}$) at the interface, the total internal electric field (E_t) was defined as $E_t = E_{ZnO/PLZT} \pm E_{dp}$ (**Figure 11**a–c). In this system, the enhanced E_t can speed up the separation and transport of carriers. Compared with the unpoled device with a responsivity of $R = 1.32$ mA W^{-1}, the devices exhibit increased ($R = 1.85$ mA W^{-1}) and decreased ($R = 1.14$ mA W^{-1}) peak responsivity in the upward and downward poling states at light intensities above 3.41 mW cm^{-2}, respectively. In addition, Pandey et al. reported the deep UV–vis PDs with a heterostructure of $SrRuO_3/BaTiO_3/ZnO/Ag$. The performance of PDs was optimized by introducing a polarization-dependent interfacial coupling effect.[103] Here, the synergistic effect of the ferroelectric field and the built-in electric field has been proven as a practical and feasible strategy to enhance the performance of PDs.

In brief, compared with doping, defect, and surface engineering, the ferroelectric field provides a non-destructive and controllable way to promote the detection ability in the ferroelectric–optoelectronic hybrid systems. Besides the ferroelectric field, other localized fields such as piezoelectric,[104] photogating,[105] and floating-gate fields,[106] can also be effective approaches toward higher-performance photodetection by improving the light–matter interaction, decreasing background noise, accelerating electron–hole separation, amplifying photo signals, etc. Meanwhile, the manipulation of localized fields can cover a broad spectrum from UV to IR. Hence, the integration of localized fields has become a promising strategy to enhance the photo-gain of PDs.

5. Ferroelectric Integrated Optoelectronic Detection Systems

As mentioned above, spontaneous polarization is due to the symmetry breaking of a unit cell and can be stabilized in two states (upward and downward polarization) by an external electric field. Effective manipulation of band bending and carrier transport can be non-destructive and controllable by introducing ferroelectrics into the optoelectronic detection systems. Currently, typical PDs integrated with ferroelectrics are homo/hetero-structures and FET structures. As for ferroelectric materials with good optoelectronic characteristics, metal–semiconductor–metal (MSM) type PDs are also very common.

5.1. Ferroelectrics Integrated Heterojunction/Homojunction Type PDs

Semiconductor junctions are promising architectures for optoelectronic conversion, which can be created by programmed up-polarized and down-polarized polarization in nanometer scales. Taking graphene as an example, the charge concentration in graphene is redistributed under a local ferroelectric field induced by varying voltages on the top or bottom gates; thus the graphene is divided into different domains (n and p type domains).[107] Another method to program ferroelectric field is the PFM technique. By using a PFM probe to switch the localized polarization, the tuned p or n-doped domains can be created without additional gate electrodes.[108,109]

© 2023 Wiley-VCH GmbH

23669608, 0, Downloaded from https://onlinelibrary.wiley.com/doi/10.1002/smtd.202300319 by Fudan University, Wiley Online Library on [28/08/2023]. See the Terms and Conditions (https://onlinelibrary.wiley.com/terms-and-conditions) on Wiley Online Library for rules of use; OA articles are governed by the applicable Creative Commons License

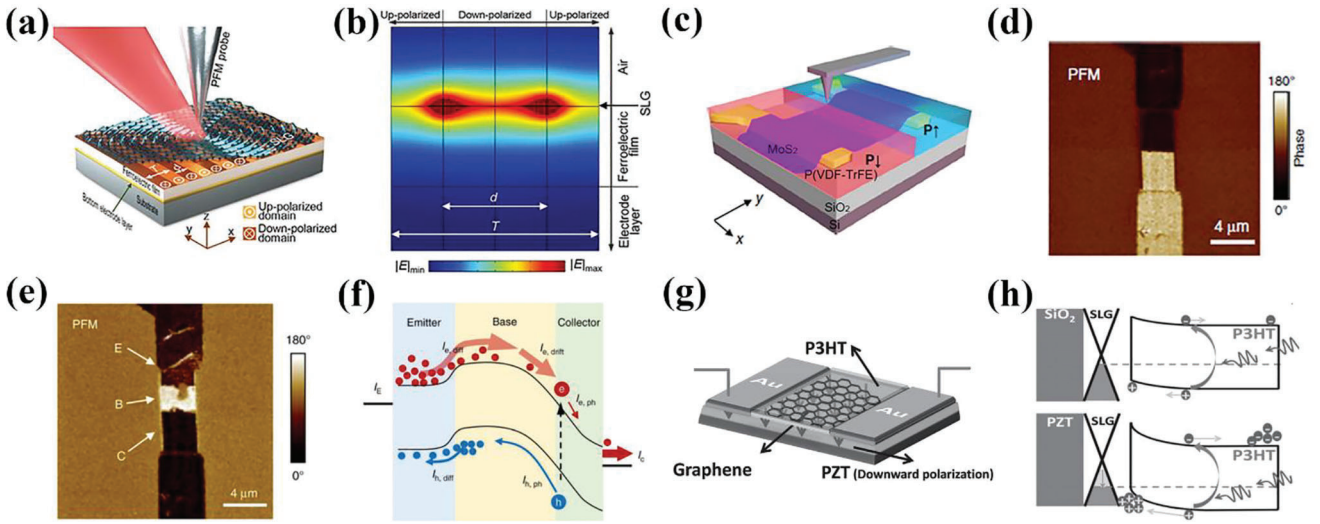

Figure 12. a) Schematic diagram of the graphene/BFO PD. b) Cross-section of electric field distribution tuned by ferroelectric domains. Reproduced with permission.[110] Copyright 2019, The Royal Society of Chemistry. c) MoS_2 p–n junction defined by AFM tip. d) PFM phase image of MoS_2 p–n junction. e) PFM phase image of MoS_2 bipolar transistor. f) The energy band diagram of the n–p–n transistor. Reproduced with permission.[88] Copyright 2019, Springer Nature. g) Schematic of a graphene/P3HT/PZT PDs. h) The energy level diagram of graphene/P3HT/PZT interface. Reproduced with permission.[111] Copyright 2014, Wiley-VCH.

As for the graphene/BFO system, the polarized states of up-polarized and down-polarized were programmed by PFM techniques. A bottom electrode was added to facilitate the switching of ferroelectric polarization (**Figure 12**a,b). Such PDs demonstrated a detectivity of ≈6.24×10^{13} Jones in the range of 5–20 μm and a responsivity up to 7.62×10^6 A W^{-1}, which is relatively high compared with common PDs.[110] The organic ferroelectric P(VDF-TrFE) was exploited to engineer the carriers doping in MoS_2 semiconducting channel. With the assistance of AFM tip as a poling electrode, the P(VDF-TrFE) film was precisely polarized into different domains with upward and downward polarization states (Figure 12c,d).[88] Further, the n–p–n bipolar transistor (the emitter, base, and collector electrodes) based on 2D MoS_2 was constructed by the ferroelectric field (Figure 12e,f), which demonstrated a photoresponse speed of ≈ 20 μs. As shown in Figure 12g,h, PZT was introduced into poly(3-hexylthiophene) (P3HT)/graphene system forming a vertical heterojunction structure.[111] The permanent surface dipoles of PZT tuned the charge migration in the channel. Under a downward polarization field, a band bending induces the transport of holes from P3HT toward graphene, effectively reducing the response time from 0.35 s/4.02 s (without polarization) to 0.18 s/1.62 s (downward polarization). It can be seen that the accumulation or depletion of charges is generally controlled by the polarization field of adjacent ferroelectric layers in ferroelectric/semiconductor systems.

5.2. Ferroelectrics Integrated FET Type PDs

FET is a widely used voltage control element that plays a significant role in many complex electronic processes,[112,113] such as logical operations, signal processing, data storage, and photodetection. The introduction of organic/inorganic ferroelectrics as gate insulators, to design and construct FET, not only effectively optimizes the performance, but also enables the miniaturization of the devices.

According to the permittivity, the dielectrics are classified into high k ($k > 3.9$) and low k ($k \leq 3.9$) dielectrics. The gate dielectrics with a high k value are good for the modulation of transport properties in channel, offering charge screening and reduced trap and impurity scattering.[94] Owing to high k value and ferroelectricity at ultra-thin scales, the HZO films emerged as a competitive candidate for integrated micro-devices. The phototransistors using MoS_2 nanoflake as the semiconducting channel and HZO film as the back gate dielectric were reported by Wang et al. (**Figure 13**a,b).[114] Based on the synergistic effect of stronger photogating and voltage amplification induced by ferroelectric negative capacitance effect, such PDs showed an ultra-steep subthreshold slope of 17.64 mV dec^{-1} and ultra-high detectivity of 4.75×10^{14} Jones. Similarly, HfO_2 has a high dielectric constant (20–25), and a wide bandgap of ≈ 5.5 eV. The 15 nm-thick HfO_2 film and 2D a-In_2Se_3 nanoflake were used as channel material and scaled gate dielectric, respectively, to prepare FET PDs. Compared with 90 nm SiO_2 as gate insulator (on/off ratio of 10^7, maximum current of 671 μA μm^{-1}), a larger on/off ratio of over 10^8 and a maximum current up to 862 μA μm^{-1} were achieved for HfO_2 integrated PDs.[115] Based on the FET structure, ferroelectrics are also combined with 2D materials to fabricate homojunction in the active layer. Wu et al. reported the preparation of $MoTe_2$ homojunction via ferroelectric polarization.[89] The organic polymer ferroelectric of P(VDF-TrFE) was used as the gate dielectric in multilayer $MoTe_2$-based FET PDs (Figure 13c,d). The doping types achieved by changing the gate bias are n–p, p–p, and n–n types in the channel (Figure 13e,f). Such PDs exhibited an on/off ratio of 5×10^5, and a detectivity up to 3×10^{12} Jones. The ferroelectric–optoelectronic systems offer a novel approach for advanced PDs and next-generation electrics.

© 2023 Wiley-VCH GmbH

23669608, 0, Downloaded from https://onlinelibrary.wiley.com/doi/10.1002/smtd.202300319 by Fudan University, Wiley Online Library on [28/08/2023]. See the Terms and Conditions (https://onlinelibrary.wiley.com/terms-and-conditions) on Wiley Online Library for rules of use; OA articles are governed by the applicable Creative Commons License

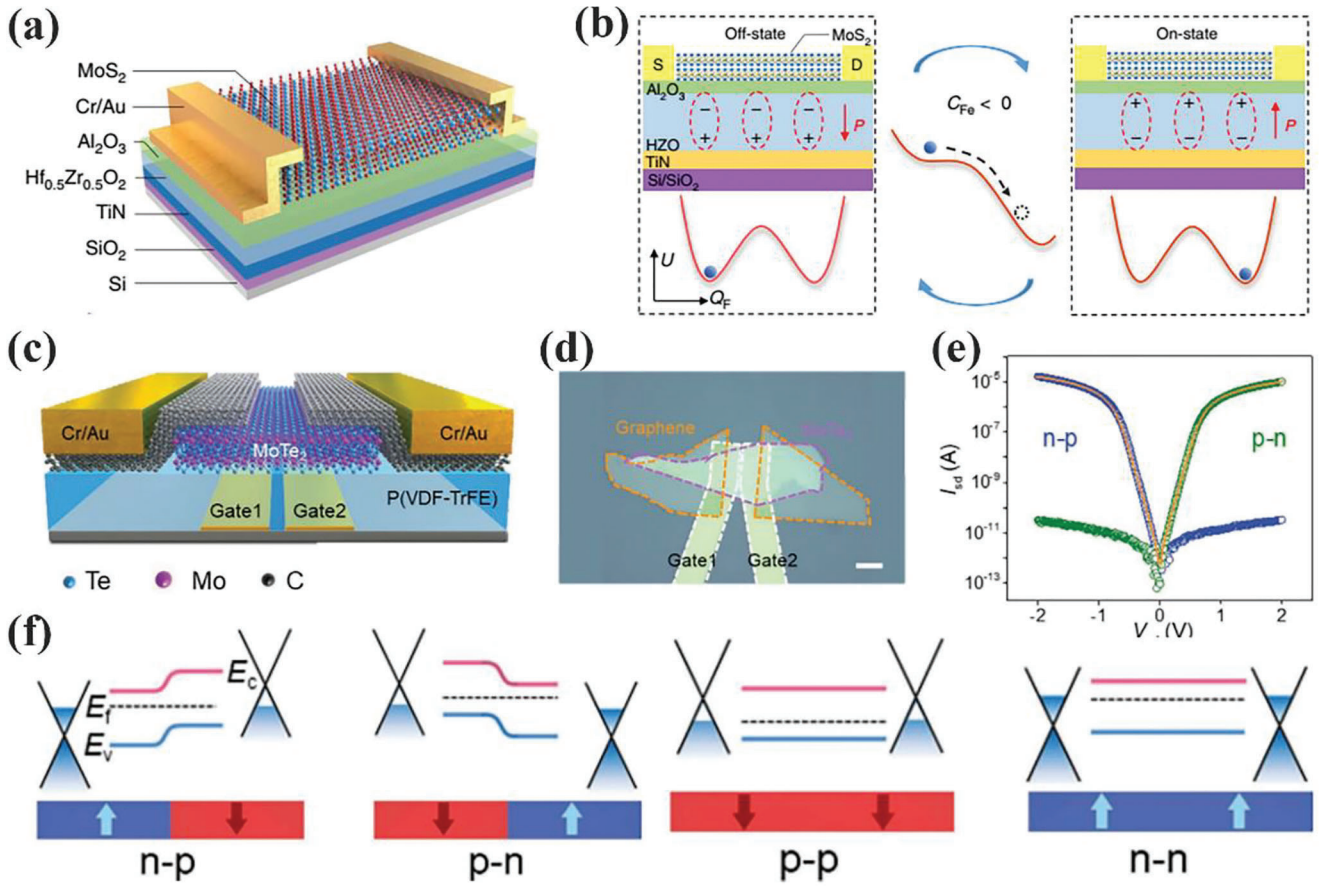

Figure 13. a) Schematic of HZO integrated MoS_2-based phototransistor. b) Ferroelectric double well energy landscapes. Reproduced with permission.[114] Copyright 2020, Springer Nature. c,d) Schematic and optical micrograph of $MoTe_2$ p–n junction PDs. e) I_{sd}–V_{sd} curves for n–p and p–n junctions. f) Schematic band diagrams for different homojunctions. Reproduced with permission.[89] Copyright 2020, Wiley-VCH.

5.3. Ferroelectrics Integrated MSM Type PDs

A class of ferroelectric materials with good photosensitive characteristics, such as organic–inorganic hybrid perovskites mentioned above, has great potential for application in polarized light or self-powered detection. As for organic–inorganic hybrid perovskites, the unique structure of periodically alternating organic and inorganic layers (natural quantum-well) results in non-linear optical and electrical properties in different crystalline phases, and the built-in electric field induced by intrinsic spontaneous polarization offers a driving force for the separation and transfer of photo-excited carriers.

According to this, Luo et al. presented self-powered visible-blind UV PDs based on hybrid perovskite $EA_4Pb_3Cl_{10}$ (EA is ethylammonium) (**Figure 14**a,b).[116] Attributed to the spontaneous polarization derived from the organic cations order–disorder transition and deformation of octahedra, the built-in electric field was generated in the active layer. A large short-circuit current of 18.6 μA cm^{-2} is higher than that of most conventional inorganic ferroelectric materials. Also, they proposed a solar-blind UV polarized-light detector based on $(isobutylammonium)_2(methylamium)Pb_2Cl_7$ (Figure 14c). The perovskite ferroelectric has a large dichroism ratio of 15.7 and a wide optical band gap of 3.27 eV.[117] Based on the bulk photovoltaic effect, such PDs presented a polarization ratio of 2.5 and a photocurrent density up to ≈ 3.6 μA cm^{-2} under a light of 266 nm (Figure 14d,e). In addition to organic–inorganic hybrid perovskites, the similar result that ferroelectric field improves the photo-responsivity of planar monolayer PDs has been obtained for α-In_2Se_3 nanoflakes.[118] Moreover, the more ferroelectrics-integrated PDs with different device structures are summarized in **Table 2**

6. Summary and Perspective

In recent years, ferroelectric-integrated electronic devices have shown significant progress in optoelectronic detection. This article reviews the recent progress of PDs based on ferroelectric–optoelectronic hybrid systems. After a brief introduction of typical optoelectronic materials, we summarized the research progress of ferroelectric materials. The structures, characteristics, atomic and molecular origin of ferroelectricity, and application in photodetection were introduced in detail. The development of 2D organic–inorganic hybrid perovskites opens up new opportunities for high-performance polarization-dependent PDs. Ultrathin 2D ferroelectrics and fluorite-structure ferroelectrics with high-*k* have laid the foundation stone for device miniaturization, which are often used as channel or gate

© 2023 Wiley-VCH GmbH

23669608, 0, Downloaded from https://onlinelibrary.wiley.com/doi/10.1002/smtd.202300319 by Fudan University, Wiley Online Library on [28/08/2023]. See the Terms and Conditions (https://onlinelibrary.wiley.com/terms-and-conditions) on Wiley Online Library for rules of use; OA articles are governed by the applicable Creative Commons License

Table 2. Parameters of ferroelectric-integrated photodetectors.

Photodetectors	Structures	Wavelength [nm]	D^* [Jones]	Bias [V]	R [AW^{-1}]	On/off ratio	Response time [t_r/t_d] [ms]	P_r [μC cm^{-2}]	E_c [kV cm^{-1}]	Ref.
Graphene/PZT/P3HT	Heterojunction	325	/	1	/	/	180/1620	/	/	[111]
P(VDF-TrFE)/MoS_2	FET	635	2.2×10^{12}	5	2570	/	1.8/2	7	22.5×10^{-3}	[85]
BTO/ZnO	Heterojunction	370	2.7×10^{11}	3	1.28×10^{-3}	14 300 (λ = 350 nm)	0.11/5.8 (λ = 350 nm)	/	2.3×10^{-3}	[98]
HZO/MoS_2	FET	637	4.75×10^{14}	0.5	96.8	/	0.4/200	10	1.5×10^{3}	[114]
PLZT/ZnO	Heterojunction	360	6.6×10^{10}	/	3.96×10^{-3}	/	40/50	34.83	/	[102]
P(VDF-TrFE)/MoS_2	n–p–n Homojunction	365	10^{13}	1	12	/	2×10^{-2}	/	5×10^{-8}	[119]
$LiNbO_3$/graphene	p–n Homojunction	1064	8.65×10^{14}	2	2.92×10^{6}	/	23/23	/	/	[120]
P(VDF-TrFE)/$MoTe_2$	FET	520	3×10^{12}	0	5	5×10^{5}	3×10^{-2}	6	15×10^{-3}	[89]
P(VDF-TrFE)/InSe	FET	532	1.63×10^{13}	3	14 250	10^{8}	0.6/1.2	/	/	[121]
In_2Se_3/WSe_2	p–n Heterojunction	650	/	−1	2.6×10^{-2}	1.24×10^{5}	2.22/2.38	/	/	[122]
$PdSe_2$/InSe	Heterojunction	1650	1×10^{10}	1	58.8	1.4	160/180	/	/	[123]
$Bi_{0.9}Eu_{0.1}FeO_3$/Nb/$SrTiO_3$	p–n Heterojunction	405	1.63×10^{10}	0	6.4×10^{-4}	2×10^{4}	50/44	/	2.7×10^{-3}/0.6×10^{-3}	[124]
BFO/graphene	Homojunction	5×10^{3}	6.24×10^{13}	/	7.62×10^{6}	/	/	/	/	[110]
α-In_2Se_3	MSM	532	/	1	2000	2×10^{7}	118/51.7	/	/	[118]
$BA_2CsPb_2Br_7$	MSM	405	1.2×10^{12}	10	3.95×10^{-2}	/	0.3/0.36	/	/	[38]
$(C_4H_9NH_3)_2(CH_3NH_3)_2Pb_3Br_{10}$	MSM	420	3.6×10^{10}	5	/	2.5×10^{3}	0.15/0.57	2.9	16	[31]

© 2023 Wiley-VCH GmbH

23669608, 0, Downloaded from https://onlinelibrary.wiley.com/doi/10.1002/smtd.202300319 by Fudan University, Wiley Online Library on [28/08/2023]. See the Terms and Conditions (https://onlinelibrary.wiley.com/terms-and-conditions) on Wiley Online Library for rules of use; OA articles are governed by the applicable Creative Commons License

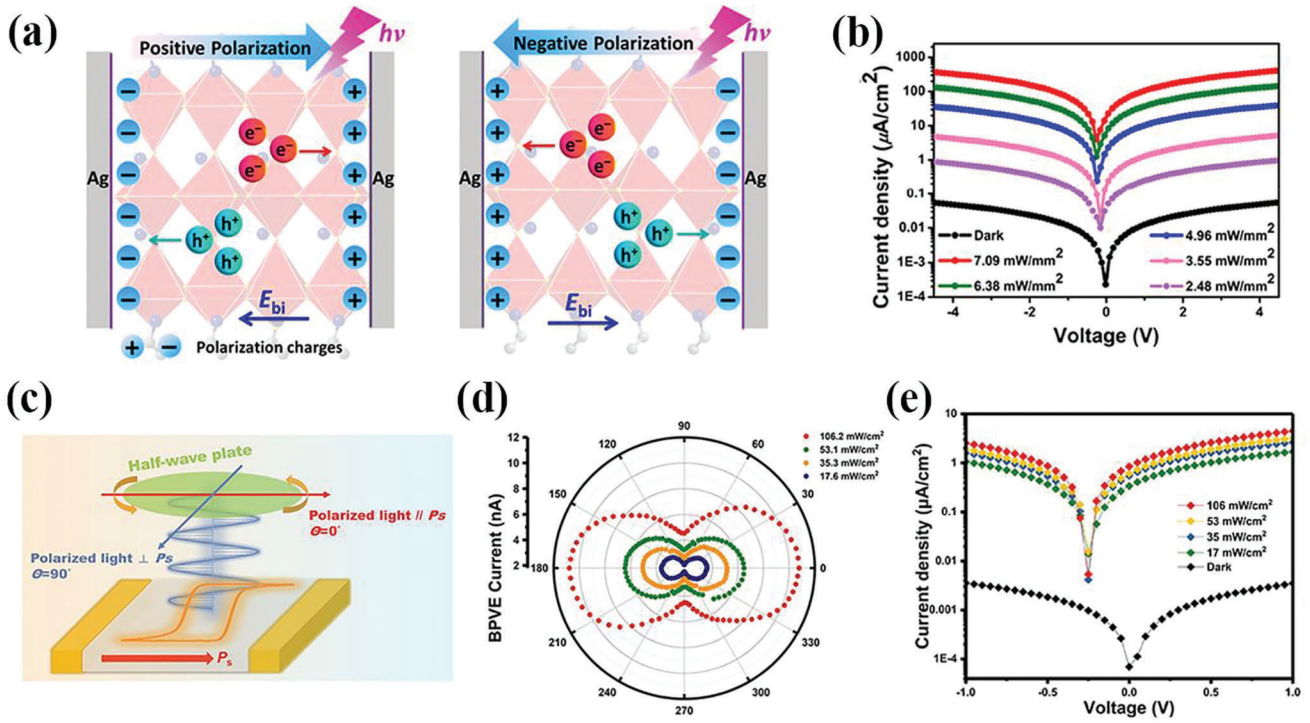

Figure 14. a) Schematic of tunable photocurrent directions. b) *J*–*V* curves under different incident light power. Reproduced with permission.[116] Copyright 2019, American Chemical Society. c) Schematic of the polarized-light PDs. d) Polar plot under different light power. e) *J*–*V* traces along *c*-axis. Reproduced with permission.[117] Copyright 2022, Wiley-VCH.

materials in transistors. Organic ferroelectrics with transparency and flexibility have natural advantages in the field of flexible electronic devices.

Subsequently, the manipulation mechanism of ferroelectric integrated hybrid system for optoelectronic detection was discussed. In nanoscale, ferroelectrics were placed in direct contact with the semiconductors. The ferroelectric field can tune the band bending at the interface between ferroelectrics and semiconductors, demonstrating the feasibility of modulating the energy band at the junction interface by ferroelectricity. The carrier motion in the active layer can be controlled by a local interfacial electrostatic field developed from a programmed ferroelectric field. Further, the ferroelectric field and built-in electric field showed synergistic interaction in ferroelectric/semiconductor heterojunction systems. Therefore, excellent performance of optoelectronic detection systems was demonstrated by the introduction of ferroelectrics.

This approach is a feasible strategy to improve the performance of electronics and shows great potential, particularly in the field of optoelectronic detection. As discussed in this article, ferroelectric integrated optoelectronic detection systems showed significant advantages, such as low dark current, broadened respond wavelength, fast response time, and low power consumption. 1) Low dark current: Ferroelectrics can effectively manipulate accumulation and depletion of charge via the synchronous polarization field programmed by gate bias, suppressing the dark current in PDs. This can improve the sensitivity of PDs, enabling them to be used in low-light detection. 2) Broadened respond wavelength: Ultra-strong ferroelectric local fields can change the bond length and bond angle of low-dimensional crystals, modifying the bandgap of optoelectronic materials. Therefore, the ferroelectric field can not only suppress the dark current and improve the detectivity of PDs, but also provides the possibility to extend their detection waveband through energy band engineering. 3) Fast response time: Ferroelectric fields have been shown to accelerate the separation of hole–electron pairs and change the distribution and transport of charge in the semiconductors, thus increasing the efficiency and response speed of PDs. This makes them highly suitable for applications that require high-speed detection, such as in communication systems. 4) Low power consumption: The non-volatile memory of ferroelectrics brings significant advantages to ferroelectric-integrated PDs. In FET type PDs, ferroelectric field plays the role of external gate bias, no external gate voltage is needed during the photodetection process and only a small drain–source bias is required to read the current flowing, resulting in an ultralow power consumption of PDs.

Although massive efforts have been devoted to understand ferroelectrics and their characteristics,[125] research on ferroelectric materials still face many challenges in the field of optoelectronics. 1) Polarization fatigue: Ferroelectrics can experience polarization fatigue over time, which degrades their performance. Also, some ferroelectrics exhibit a strong temperature-dependent polarization. These limit their usefulness in certain applications that require long-term stability and reliability. 2) Critical size effect: When the size of the ferroelectrics is below the critical size, the symmetry of the crystal structure changes, leading to a weakening or disappearance of the ferroelectric properties. While ultrathin ferroelectric materials have shown great potential for

© 2023 Wiley-VCH GmbH

23669608, 0, Downloaded from https://onlinelibrary.wiley.com/doi/10.1002/smtd.202300319 by Fudan University, Wiley Online Library on [28/08/2023]. See the Terms and Conditions (https://onlinelibrary.wiley.com/terms-and-conditions) on Wiley Online Library for rules of use; OA articles are governed by the applicable Creative Commons License

various applications, they still face significant challenges when it comes to device miniaturization, particularly those with perovskite structure. 3) Fabrication complexity: Integrating ferroelectrics with PDs can be challenging, as it requires precise deposition and good interface contact between two materials, which increases the complexity and cost of the fabrication process.

These challenges highlight the need for continued research and development in the area of ferroelectric integrated optoelectronic detection systems, with a particular emphasis on the strategies for sub-nanometer size and mitigating polarization fatigue of ferroelectrics to match device design and developing more efficient and cost-effective fabrication methods. Additionally, the manipulation mechanism of the carrier types derived from ferroelectric polarization and the interaction between semiconductors and ferroelectrics need to be further investigated. On the other hand, ultrathin semiconductor materials with good crystalline quality are particularly well-suited for manipulation under ferroelectric local field. With a deep understanding and extensive research on ferroelectric materials, devices integrated with ferroelectrics will provide new cutting-edge solutions to further advance in the field of optoelectronic detection.

Acknowledgements

J.L., L.S., and X.L.Z. contributed equally to this work. The authors acknowledge financial support from the Ministry of Science and Technology of the People's Republic of China (no. 2022YFA1402904), National Natural Science Foundation of China (nos. 12061131009, 12211530438, and 92263106), and Science and Technology Commission of Shanghai Municipality (nos. 21520712600 and 19520744300). D.V.S. gratefully acknowledges the financial support from the Russian Science Foundation (No. 21-49-00039).

Conflict of Interest

The authors declare no conflict of interest.

Keywords

ferroelectrics, field-effect transistors, heterostructures, hybrid systems, optoelectronic materials, photodetection

Received: March 12, 2023
Revised: April 28, 2023
Published online:

[1] G. Wu, B. Tian, L. Liu, W. Lv, S. Wu, X. Wang, Y. Chen, J. Li, Z. Wang, S. Wu, H. Shen, T. Lin, P. Zhou, Q. Liu, C. Duan, S. Zhang, X. Meng, S. Wu, W. Hu, X. Wang, J. Chu, J. Wang, *Nat. Electron.* **2020**, *3*, 43.
[2] J. Wang, Y. Xing, F. Wan, C. Fu, C.-H. Xu, F.-X. Liang, L.-B. Luo, *J. Mater. Chem. C* **2022**, *10*, 12929.
[3] H. Wang, Z. Li, D. Li, P. Chen, L. Pi, X. Zhou, T. Zhai, *Adv. Funct. Mater.* **2021**, *31*, 2103106.
[4] W. Ouyang, J. Chen, Z. Shi, X. S. Fang, *Appl. Phys. Rev.* **2021**, *8*, 031315.
[5] F. Wang, X. Zou, M. Xu, H. Wang, H. Wang, H. Guo, J. Guo, P. Wang, M. Peng, Z. Wang, Y. Wang, J. Miao, F. Chen, J. Wang, X. Chen, A. Pan, C. Shan, L. Liao, W. Hu, *Adv. Sci.* **2021**, *8*, 2100569.
[6] D. Yang, D. Ma, *Adv. Opt. Mater.* **2019**, *7*, 1800522.
[7] S. Cai, X. Xu, W. Yang, J. Chen, X. S. Fang, *Adv. Mater.* **2019**, *31*, 1808138.
[8] F. Cao, Z. Li, X. Liu, Z. Shi, X. S. Fang, *Adv. Funct. Mater.* **2022**, *32*, 2206151.
[9] F. Cao, T. Yan, Z. Li, L. Wu, X. S. Fang, *Adv. Opt. Mater.* **2022**, *10*, 2200786.
[10] Y. H. Chen, L. X. Su, M. M. Jiang, X. S. Fang, *J. Mater. Sci. Technol.* **2022**, *105*, 259.
[11] Q. Hao, H. Yi, J. Liu, Y. Wang, J. Chen, X. Yin, C. S. Tang, D. Qi, H. Gan, A. T. S. Wee, Y. Chai, W. Zhang, *Adv. Opt. Mater.* **2022**, *10*, 2200063.
[12] K. Y. Thai, I. Park, B. J. Kim, A. T. Hoang, Y. Na, C. U. Park, Y. Chae, J. H. Ahn, *ACS Nano* **2021**, *15*, 12836.
[13] W. Wang, W. Zhao, H. Xu, S. Liu, W. Huang, Q. Zhao, *Coord. Chem. Rev.* **2021**, *429*, 213616.
[14] J. L. K. Chang, H. Lin, N. Wang, K. Zhao, A. Zhang, F. Jin, Y. Zhong, X. Hu, W. Duan, Q. Zhang, L. Fu, Q.-K. Xue, X. Chen, S.-H. Ji, *Science* **2016**, *353*, 274.
[15] Y. Sun, G. Niu, W. Ren, X. Meng, J. Zhao, W. Luo, Z. G. Ye, Y. H. Xie, *ACS Nano* **2021**, *15*, 10982.
[16] T. Jin, J. Mao, J. Gao, C. Han, K. P. Loh, A. T. S. Wee, W. Chen, *ACS Nano* **2022**, *16*, 13595.
[17] J. Miao, W. Hu, N. Guo, Z. Lu, X. Zou, L. Liao, S. Shi, P. Chen, Z. Fan, J. C. Ho, T. X. Li, X. S. Chen, W. Lu, *ACS Nano* **2014**, *8*, 3628.
[18] X. Liu, S. Hu, Z. Lin, X. Li, L. Song, W. Yu, Q. Wang, W. He, *ACS Appl. Mater. Interfaces* **2021**, *13*, 15820.
[19] H. Jang, D.-K. Kwon, D. H. Kim, J.-M. Myoung, *J. Mater. Chem. C* **2022**, *10*, 6805.
[20] W. Ouyang, F. Teng, X. S. Fang, *Adv. Funct. Mater.* **2018**, *28*, 1707178.
[21] J. Liu, J. Liu, C. Wang, Z. Ge, D. Wang, L. Xia, L. Guo, N. Du, X. Hao, H. Xiao, *Sol. Energy Mater. Sol. Cells* **2020**, *208*, 110380.
[22] J. Liu, C. Wang, Z. Ge, T. Wang, L. Xia, Y. Wu, N. Du, H. Xiao, J. Liu, *Opt. Mater.* **2020**, *107*, 110059.
[23] X. Chen, K. Shehzad, L. Gao, M. Long, H. Guo, S. Qin, X. Wang, F. Wang, Y. Shi, W. Hu, Y. Xu, X. Wang, *Adv. Mater.* **2020**, *32*, 1902039.
[24] Q. A. Vu, J. H. Lee, V. L. Nguyen, Y. S. Shin, S. C. Lim, K. Lee, J. Heo, S. Park, K. Kim, Y. H. Lee, W. J. Yu, *Nano Lett.* **2017**, *17*, 453.
[25] M. Massicotte, P. Schmidt, F. Vialla, K. G. Schadler, A. Reserbat-Plantey, K. Watanabe, T. Taniguchi, K. J. Tielrooij, F. H. Koppens, *Nat. Nanotechnol.* **2016**, *11*, 42.
[26] K. Zhang, X. Fang, Y. Wang, Y. Wan, Q. Song, W. Zhai, Y. Li, G. Ran, Y. Ye, L. Dai, *ACS Appl. Mater. Interfaces* **2017**, *9*, 5392.
[27] S. Hong, S. Baek, T. T. T. Can, W. S. Choi, S. Kim, *Adv. Electron. Mater.* **2022**, *8*, 2101063.
[28] D. Zheng, X. Dong, J. Lu, Y. Niu, H. Wang, *Small* **2022**, *18*, 2105188.
[29] L. Protesescu, S. Yakunin, M. I. Bodnarchuk, F. Krieg, R. Caputo, C. H. Hendon, R. X. Yang, A. Walsh, M. V. Kovalenko, *Nano Lett.* **2015**, *15*, 3692.
[30] E. Hong, Z. Li, T. Yan, X. S. Fang, *Nano Lett.* **2022**, *22*, 8662.
[31] L. Li, Z. Sun, P. Wang, W. Hu, S. Wang, C. Ji, M. Hong, J. Luo, *Angew. Chem., Int. Ed.* **2017**, *56*, 12150.
[32] Y. Wang, L. Zhu, Y. Hu, Z. Deng, Z. Lou, Y. Hou, F. Teng, *Opt. Express* **2017**, *25*, 7719.
[33] M. T. X. Gong, Y. Xia, W. Cai, J. S. Moon, Y. Cao, G. Yu, C.-L. Shieh, B. Nilsson, A. J. Heeger, *Science* **2009**, *325*, 1665.
[34] Z.-X. Liu, T.-K. Lau, G. Zhou, S. Li, J. Ren, S. K. Das, R. Xia, G. Wu, H. Zhu, X. Lu, H.-L. Yip, H. Chen, C.-Z. Li, *Nano Energy* **2019**, *63*, 103807.
[35] P. S. A. Lipatov, A. Gruverman, A. Sinitskii, *ACS Nano* **2015**, *9*, 8089.
[36] W. Q. Liao, Y. Zhang, C. L. Hu, J. G. Mao, H. Y. Ye, P. F. Li, S. D. Huang, R. G. Xiong, *Nat. Commun.* **2015**, *6*, 7338.
[37] L. Li, X. Liu, Y. Li, Z. Xu, Z. Wu, S. Han, K. Tao, M. Hong, J. Luo, Z. Sun, *J. Am. Chem. Soc.* **2019**, *141*, 2623.

© 2023 Wiley-VCH GmbH

23669608, 0, Downloaded from https://onlinelibrary.wiley.com/doi/10.1002/smtd.202300319 by Fudan University, Wiley Online Library on [28/08/2023]. See the Terms and Conditions (https://onlinelibrary.wiley.com/terms-and-conditions) on Wiley Online Library for rules of use; OA articles are governed by the applicable Creative Commons License

[38] J. Wang, Y. Liu, S. Han, Y. Ma, Y. Li, Z. Xu, J. Luo, M. Hong, Z. Sun, *Sci. Bull.* **2021**, *66*, 158.
[39] L. Su, Z. Li, F. Cao, X. Liu, X. S. Fang, *J. Mater. Chem. C* **2022**, *10*, 9035.
[40] X. Li, S. Chen, P. F. Liu, Y. Zhang, Y. Chen, H. L. Wang, H. Yuan, S. Feng, *J. Am. Chem. Soc.* **2020**, *142*, 3316.
[41] E. H. Smith, N. A. Benedek, C. J. Fennie, *Inorg. Chem.* **2015**, *54*, 8536.
[42] H. Y. Zhang, Y. Y. Tang, P. P. Shi, R. G. Xiong, *Acc. Chem. Res.* **2019**, *52*, 1928.
[43] F. Jia, S. Hu, S. Xu, H. Gao, G. Zhao, P. Barone, A. Stroppa, W. Ren, *J. Phys. Chem. Lett.* **2020**, *11*, 5177.
[44] K. Leng, R. Li, S. P. Lau, K. P. Loh, *Trends Chem* **2021**, *3*, 716.
[45] C. Ji, Y. Li, X. Liu, Y. Wang, T. Zhu, Q. Chen, L. Li, S. Wang, J. Luo, *Angew. Chem., Int. Ed.* **2021**, *60*, 20970.
[46] S. S. Cheema, D. Kwon, N. Shanker, R. D. Reis, S. L. Hsu, J. Xiao, H. Zhang, R. Wagner, A. Datar, M. R. McCarter, C. R. Serrao, A. K. Yadav, G. Karbasian, C. H. Hsu, A. J. Tan, L. C. Wang, V. Thakare, X. Zhang, A. Mehta, E. Karapetrova, R. V. Chopdekar, P. Shafer, E. Arenholz, C. Hu, R. Proksch, R. Ramesh, J. Ciston, S. Salahuddin, *Nature* **2020**, *580*, 478.
[47] M. Trieloff, E. K. Jessberger, I. Herrwerth, J. Hopp, C. Fiéni, M. Ghélis, M. Bourot-Denise, P. Pellas, *Nature* **2003**, *422*, 502.
[48] T. S. Böscke, J. Müller, D. Bräuhaus, U. Schröder, U. Böttger, *Appl. Phys. Lett.* **2011**, *99*, 102903.
[49] X. Sang, E. D. Grimley, T. Schenk, U. Schroeder, J. M. LeBeau, *Appl. Phys. Lett.* **2015**, *106*, 162905.
[50] M. H. Park, T. Schenk, C. M. Fancher, E. D. Grimley, C. Zhou, C. Richter, J. M. LeBeau, J. L. Jones, T. Mikolajick, U. Schroeder, *J. Mater. Chem. C* **2017**, *5*, 4677.
[51] P. N. Y. Wei, M. Salverda, S. Matzen, H. J. Zhao, J. Momand, A. Everhardt, G. R. Blake, P. Lecoeur, B. J. Kooi, J. Íñiguez, B. Dkhil, B. Noheda, *Nat. Mater.* **2018**, *17*, 1095.
[52] D. H. Lee, Y. Lee, K. Yang, J. Y. Park, S. H. Kim, P. R. S. Reddy, M. Materano, H. Mulaosmanovic, T. Mikolajick, J. L. Jones, U. Schroeder, M. H. Park, *Appl. Phys. Rev.* **2021**, *8*, 021312.
[53] M. Materano, T. Mittmann, P. D. Lomenzo, C. Zhou, J. L. Jones, M. Falkowski, A. Kersch, T. Mikolajick, U. Schroeder, A. C. S. Appl, *Electron. Mater.* **2020**, *2*, 3618.
[54] M. H. Park, Y. H. Lee, C. S. Hwang, *Nanoscale* **2019**, *11*, 19477.
[55] M. H. Park, Y. H. Lee, T. Mikolajick, U. Schroeder, C. S. Hwang, *Adv. Electron. Mater.* **2019**, *5*, 1800522.
[56] D. Kwon, S. Cheema, N. Shanker, K. Chatterjee, Y.-H. Liao, A. J. Tan, C. Hu, S. Salahuddin, *IEEE Electron Device Lett.* **2019**, *40*, 993.
[57] F. Liu, L. You, K. L. Seyler, X. Li, P. Yu, J. Lin, X. Wang, J. Zhou, H. Wang, H. He, S. T. Pantelides, W. Zhou, P. Sharma, X. Xu, P. M. Ajayan, J. Wang, Z. Liu, *Nat. Commun.* **2016**, *7*, 12357.
[58] Z. Guan, H. Hu, X. Shen, P. Xiang, N. Zhong, J. Chu, C. Duan, *Adv. Electron. Mater.* **2019**, *6*, 1800522.
[59] N. Balke, S. M. Neumayer, J. A. Brehm, M. A. Susner, B. J. Rodriguez, S. Jesse, S. V. Kalinin, S. T. Pantelides, M. A. McGuire, P. Maksymovych, *ACS Appl. Mater. Interfaces* **2018**, *10*, 27188.
[60] A. Belianinov, Q. He, A. Dziaugys, P. Maksymovych, E. Eliseev, A. Borisevich, A. Morozovska, J. Banys, Y. Vysochanskii, S. V. Kalinin, *Nano Lett.* **2015**, *15*, 3808.
[61] M. Chyasnavichyus, M. A. Susner, A. V. Ievlev, E. A. Eliseev, S. V. Kalinin, N. Balke, A. N. Morozovska, M. A. McGuire, P. Maksymovych, *Appl. Phys. Lett.* **2016**, *109*, 172901.
[62] Y. Zhou, D. Wu, Y. Zhu, Y. Cho, Q. He, X. Yang, K. Herrera, Z. Chu, Y. Han, M. C. Downer, H. Peng, K. Lai, *Nano Lett.* **2017**, *17*, 5508.
[63] W. Tang, X. Zhang, H. Yu, L. Gao, Q. Zhang, X. Wei, M. Hong, L. Gu, Q. Liao, Z. Kang, Z. Zhang, Y. Zhang, *Small Methods* **2022**, *6*, 2101583.
[64] K. Chang, T. P. Kaloni, H. Lin, A. Bedoya-Pinto, A. K. Pandeya, I. Kostanovskiy, K. Zhao, Y. Zhong, X. Hu, Q. K. Xue, X. Chen, S. H. Ji, S. Barraza-Lopez, S. S. P. Parkin, *Adv. Mater.* **2019**, *31*, 1804428.
[65] K. Liu, J. Lu, S. Picozzi, L. Bellaiche, H. Xiang, *Phys. Rev. Lett.* **2018**, *121*, 027601.
[66] J. Sławińska, F. T. Cerasoli, H. Wang, S. Postorino, A. Supka, S. Curtarolo, M. Fornari, M. B. Nardelli, *2D Mater.* **2019**, *6*, 025012.
[67] J. Sławińska, F. T. Cerasoli, P. Gopal, M. Costa, S. Curtarolo, M. B. Nardelli, *2D Mater.* **2020**, *7*, 025026.
[68] X.-W. Shen, Y.-W. Fang, B.-B. Tian, C.-G. Duan, *ACS Appl. Electron. Mater.* **2019**, *1*, 1133.
[69] Y. Yan, Q. Deng, S. Li, T. Guo, X. Li, Y. Jiang, X. Song, W. Huang, J. Yang, C. Xia, *Nanoscale* **2021**, *13*, 16122.
[70] W. C. Yap, Z. Yang, M. Mehboudi, J.-A. Yan, S. Barraza-Lopez, W. Zhu, *Nano Res.* **2017**, *11*, 420.
[71] Y. Chen, X. Wang, L. Huang, X. Wang, W. Jiang, Z. Wang, P. Wang, B. Wu, T. Lin, H. Shen, Z. Wei, W. Hu, X. Meng, J. Chu, J. Wang, *Nat. Commun.* **2021**, *12*, 4030.
[72] W. Ding, J. Zhu, Z. Wang, Y. Gao, D. Xiao, Y. Gu, Z. Zhang, W. Zhu, *Nat. Commun.* **2017**, *8*, 14956.
[73] F. Xue, W. Hu, K. C. Lee, L. S. Lu, J. Zhang, H. L. Tang, A. Han, W. T. Hsu, S. Tu, W. H. Chang, C. H. Lien, J. H. He, Z. Zhang, L. J. Li, X. Zhang, *Adv. Funct. Mater.* **2018**, *28*, 1803738.
[74] S. Wan, Y. Li, W. Li, X. Mao, W. Zhu, H. Zeng, *Nanoscale* **2018**, *10*, 14885.
[75] Y. T. Huang, N. K. Chen, Z. Z. Li, X. P. Wang, H. B. Sun, S. Zhang, X. B. Li, *InfoMat* **2022**, *4*, e12341.
[76] S. Wan, Y. Li, W. Li, X. Mao, C. Wang, C. Chen, J. Dong, A. Nie, J. Xiang, Z. Liu, W. Zhu, H. Zeng, *Adv. Funct. Mater.* **2019**, *29*, 1808606.
[77] H. Kawai, *J. Appl. Phys.* **1969**, *8*, 975.
[78] J. G. Bergman, J. H. McFee, G. R. Crane, *Appl. Phys. Lett.* **1971**, *18*, 203.
[79] R. G. Kepler, R. A. Anderson, *J. Appl. Phys.* **1978**, *49*, 1232.
[80] T. Furukawa, M. Date, E. Fukada, *J. Appl. Phys.* **1980**, *51*, 1135.
[81] B. Stadlober, M. Zirkl, M. Irimia-Vladu, *Chem. Soc. Rev.* **2019**, *48*, 1787.
[82] L. Li, M. Zhang, M. Rong, W. Ruan, *RSC Adv.* **2014**, *4*, 3938.
[83] E. Kabir, M. Khatun, L. Nasrin, M. J. Raihan, M. Rahman, *J. Phys. D: Appl. Phys.* **2017**, *50*, 163002.
[84] W. J. Hu, D. M. Juo, L. You, J. Wang, Y. C. Chen, Y. H. Chu, T. Wu, *Sci. Rep.* **2014**, *4*, 4772.
[85] X. Wang, P. Wang, J. Wang, W. Hu, X. Zhou, N. Guo, H. Huang, S. Sun, H. Shen, T. Lin, M. Tang, L. Liao, A. Jiang, J. Sun, X. Meng, X. Chen, W. Lu, J. Chu, *Adv. Mater.* **2015**, *27*, 6575.
[86] J. F. Legrand, *Ferroelectrics* **1989**, *91*, 303.
[87] G.-d. Kang, Y.-m. Cao, *J. Membr. Sci.* **2014**, *463*, 145.
[88] L. Lv, F. Zhuge, F. Xie, X. Xiong, Q. Zhang, N. Zhang, Y. Huang, T. Zhai, *Nat. Commun.* **2019**, *10*, 3331.
[89] G. Wu, X. Wang, Y. Chen, S. Wu, B. Wu, Y. Jiang, H. Shen, T. Lin, Q. Liu, X. Wang, P. Zhou, S. Zhang, W. Hu, X. Meng, J. Chu, J. Wang, *Adv. Mater.* **2020**, *32*, 1907937.
[90] D. Zheng, H. Fang, P. Wang, W. Luo, F. Gong, J. C. Ho, X. Chen, W. Lu, L. Liao, J. Wang, W. Hu, *Adv. Funct. Mater.* **2016**, *26*, 7690.
[91] D. Zheng, J. Wang, W. Hu, L. Liao, H. Fang, N. Guo, P. Wang, F. Gong, X. Wang, Z. Fan, X. Wu, X. Meng, X. Chen, W. Lu, *Nano Lett.* **2016**, *16*, 2548.
[92] K. Maity, U. Pal, H. K. Mishra, P. Maji, P. Sadhukhan, Z. Mallick, S. Das, B. Mondal, D. Mandal, *Nano Energy* **2022**, *92*, 106743.
[93] Y. Li, X.-Y. Sun, C.-Y. Xu, J. Cao, Z.-Y. Sun, L. Zhen, *Nanoscale* **2018**, *10*, 23080.
[94] Y. Sun, G. Niu, W. Ren, X. Meng, J. Zhao, W. Luo, Z.-G. Ye, Y.-H. Xie, *ACS Nano* **2021**, *15*, 10982.
[95] L. Li, Y. Zhang, R. Wang, J. Sun, Y. Si, H. Wang, C. Pan, Y. Dai, *Nano Energy* **2019**, *65*, 104046.

© 2023 Wiley-VCH GmbH

23669608, 0, Downloaded from https://onlinelibrary.wiley.com/doi/10.1002/smtd.202300319 by Fudan University, Wiley Online Library on [28/08/2023]. See the Terms and Conditions (https://onlinelibrary.wiley.com/terms-and-conditions) on Wiley Online Library for rules of use; OA articles are governed by the applicable Creative Commons License

[96] H. Lee, T. H. Kim, J. J. Patzner, H. Lu, J.-W. Lee, H. Zhou, W. Chang, M. K. Mahanthappa, E. Y. Tsymbal, A. Gruverman, C.-B. Eom, *Nano Lett.* **2016**, *16*, 2400.
[97] R. Guo, L. Shen, H. Wang, Z. Lim, W. Lu, P. Yang, Ariando, A. Gruverman, T. Venkatesan, Y. P. Feng, J. Chen, *Adv. Mater. Interfaces* **2016**, *3*, 1600737.
[98] Y. Zhang, X. Zhao, J. Chen, S. Li, W. Yang, X. S. Fang, *Adv. Funct. Mater.* **2020**, *30*, 1907650.
[99] Y. Sun, D. Xie, X. Zhang, J. Xu, X. Li, X. Li, R. Dai, X. Li, P. Li, X. Gao, H. Zhu, *Nanotechnology* **2017**, *28*, 045204.
[100] X. Zhou, Q. Ke, S. Tang, J. Luo, Z. Lu, *J. Energy Chem.* **2023**, *77*, 487.
[101] Y. Zhang, J. Chen, Q. Zhang, Y. Lu, H. Huang, Y. He, *J. Am. Ceram. Soc.* **2022**, *105*, 392.
[102] J. Chen, Z. Wang, H. He, J. Mao, Y. Zhang, Q. Zhang, M. Li, Y. Lu, Y. He, *Adv. Electron. Mater.* **2021**, *7*, 2100717.
[103] B. K. Pandey, S. Dias, K. K. Nanda, S. B. Krupanidhi, *J. Appl. Phys.* **2017**, *122*, 234502.
[104] H. Wang, J. Ma, L. Cong, H. Zhou, P. Li, L. Fei, B. Li, H. Xu, Y. Liu, *Mater. Today Phys.* **2021**, *20*, 100464.
[105] H. Fang, W. Hu, *Adv. Sci.* **2017**, *4*, 1700323.
[106] F. Gong, W. Luo, J. Wang, P. Wang, H. Fang, D. Zheng, N. Guo, J. Wang, M. Luo, J. C. Ho, X. Chen, W. Lu, L. Liao, W. Hu, *Adv. Funct. Mater.* **2016**, *26*, 6084.
[107] J. C. W. S. Nathaniel, M. Gabor, Q. Ma, N. L. Nair, T. Taychatanapat, K. Watanabe, T. Taniguchi, L. S. Levitov, P. Jarillo-Herrero, *Science* **2011**, *334*, 648.
[108] Y. Liu, X. Zhang, C. Cao, Y. Zhang, J. Wei, Y. j. Li, W. Liang, Z. Hu, J. Zhang, Y. Wei, X. Deng, *Adv. Funct. Mater.* **2017**, *27*, 1703771.
[109] C. Wang, X. Ke, J. Wang, R. Liang, Z. Luo, Y. Tian, D. Yi, Q. Zhang, J. Wang, X. F. Han, G. Van Tendeloo, L. Q. Chen, C. W. Nan, R. Ramesh, J. Zhang, *Nat. Commun.* **2016**, *7*, 10636.
[110] J. Guo, Y. Liu, Y. Lin, Y. Tian, J. Zhang, T. Gong, T. Cheng, W. Huang, X. Zhang, *Nanoscale* **2019**, *11*, 20868.
[111] W.-C. Tan, W.-H. Shih, Y. F. Chen, *Adv. Funct. Mater.* **2014**, *24*, 6818.
[112] A. I. Khan, K. Chatterjee, B. Wang, S. Drapcho, L. You, C. Serrao, S. R. Bakaul, R. Ramesh, S. Salahuddin, *Nat. Mater.* **2015**, *14*, 182.
[113] S. Salahuddin, S. Datta, *Nano Lett.* **2008**, *8*, 405.
[114] L. Tu, R. Cao, X. Wang, Y. Chen, S. Wu, F. Wang, Z. Wang, H. Shen, T. Lin, P. Zhou, X. Meng, W. Hu, Q. Liu, J. Wang, M. Liu, J. Chu, *Nat. Commun.* **2020**, *11*, 101.
[115] M. Si, A. K. Saha, S. Gao, G. Qiu, J. Qin, Y. Duan, J. Jian, C. Niu, H. Wang, W. Wu, S. K. Gupta, P. D. Ye, *Nat. Electron.* **2019**, *2*, 580.
[116] S. Wang, L. Li, W. Weng, C. Ji, X. Liu, Z. Sun, W. Lin, M. Hong, J. Luo, *J. Am. Chem. Soc.* **2020**, *142*, 55.
[117] L. Lu, W. Weng, Y. Ma, Y. Liu, S. Han, X. Liu, H. Xu, W. Lin, Z. Sun, J. Luo, *Angew. Chem., Int. Ed.* **2022**, *61*, 202205030.
[118] P. Hou, Y. Lv, X. Zhong, J. Wang, A. C. S. Appl, *Nano Mater.* **2019**, *2*, 4443.
[119] L. Lv, F. Zhuge, F. Xie, X. Xiong, Q. Zhang, N. Zhang, Y. Huang, T. Zhai, *Nat. Commun.* **2019**, *10*, 3331.
[120] H. Guan, J. Hong, X. Wang, J. Ming, Z. Zhang, A. Liang, X. Han, J. Dong, W. Qiu, Z. Chen, H. Lu, H. Zhang, *Adv. Opt. Mater.* **2021**, *9*, 2100245.
[121] L. Liu, L. Wu, A. Wang, H. Liu, R. Ma, K. Wu, J. Chen, Z. Zhou, Y. Tian, H. Yang, C. Shen, L. Bao, Z. Qin, S. T. Pantelides, H.-J. Gao, *Nano Lett.* **2020**, *20*, 6666.
[122] B. Liu, B. Tang, F. Lv, Y. Zeng, J. Liao, S. Wang, Q. Chen, *Nanotechnology* **2020**, *31*, 065203.
[123] W. Ahmad, J. Liu, J. Jiang, Q. Hao, D. Wu, Y. Ke, H. Gan, V. Laxmi, Z. Ouyang, F. Ouyang, Z. Wang, F. Liu, D. Qi, W. Zhang, *Adv. Funct. Mater.* **2021**, *31*, 2104143.
[124] M. Wei, J. Hao, M. Liu, L. Yang, Y. Xie, X. Wang, Z. Li, Y. Su, Z. Hu, J.-M. Liu, *J. Alloys Compd.* **2022**, *915*, 165451.
[125] L. Su, T. T. Yan, X. Y. Liu, F. Cao, X. S. Fang, *Adv. Funct. Mater.* **2023**, *33*, 2214533.

 © 2023 Wiley-VCH GmbH

23669608, 0, Downloaded from https://onlinelibrary.wiley.com/doi/10.1002/smtd.202300319 by Fudan University, Wiley Online Library on [28/08/2023]. See the Terms and Conditions (https://onlinelibrary.wiley.com/terms-and-conditions) on Wiley Online Library for rules of use; OA articles are governed by the applicable Creative Commons License